

Three Learning Stages and Accuracy-Efficiency Tradeoff of Restricted Boltzmann Machines

Lennart Dabelow¹ and Masahito Ueda^{2,1}

¹RIKEN Center for Emergent Matter Science (CEMS), Wako, Saitama 351-0198, Japan

²Department of Physics and Institute for Physics of Intelligence,

Graduate School of Science, The University of Tokyo, Bunkyo-ku, Tokyo 113-0033, Japan

(Dated: September 5, 2022)

Restricted Boltzmann Machines (RBMs) offer a versatile architecture for unsupervised machine learning that can in principle approximate any target probability distribution with arbitrary accuracy. However, the RBM model is usually not directly accessible due to its computational complexity, and Markov-chain sampling is invoked to analyze the learned probability distribution. For training and eventual applications, it is thus desirable to have a sampler that is both accurate and efficient. We highlight that these two goals generally compete with each other and cannot be achieved simultaneously. More specifically, we identify and quantitatively characterize three regimes of RBM learning: independent learning, where the accuracy improves without losing efficiency; correlation learning, where higher accuracy entails lower efficiency; and degradation, where both accuracy and efficiency no longer improve or even deteriorate. These findings are based on numerical experiments and heuristic arguments.

Restricted Boltzmann Machines (RBMs) [1, 2] are a versatile and conceptionally simple unsupervised machine learning model. Besides traditional applications, such as dimensional reduction and pretraining [3–6] and text classification [7], they have become increasingly widespread in the physics community [8, 9]. Examples include tomography [7, 11] and variational encoding [12–18] of quantum states, time-series forecasting [19], and information-based renormalization group transformations [20, 21].

A general goal in unsupervised machine learning is to find the best representation of some unknown *target probability distribution* $p(x)$ within a family of *model distributions* $\hat{p}_\theta(x)$, where θ denotes the model parameters to be optimized. To this end, the RBM architecture introduces two types of *units*, the *visible* units $x = (x_1, \dots, x_M) \in \mathcal{X}$, which relate to the states of the target distribution, and the *hidden* units $h = (h_1, \dots, h_N) \in \mathcal{H}$, which mediate correlations between the visible units (see, e.g., Refs. [2, 4, 5] for reviews and the top-right corner of Fig. 1 for an illustration). We focus on the most common case where both the visible and the hidden units are binary, i.e., $\mathcal{X} = \{0, 1\}^M$ and $\mathcal{H} = \{0, 1\}^N$. The RBM model is based on a joint Boltzmann distribution for x and h ,

$$\hat{p}_\theta(x, h) := Z_\theta^{-1} e^{-E_\theta(x, h)}, \quad (1)$$

where the “energy” $E_\theta(x, h) := -\sum_{i,j} w_{ij} x_i h_j - \sum_i a_i x_i - \sum_j b_j h_j$ takes the form of a classical spin Hamiltonian with “interactions” between visible and hidden units described by the *weights* $w_{ij} \in \mathbb{R}$ and “external fields” for visible and hidden units described by the *biases* $a_i, b_j \in \mathbb{R}$. The weights and biases constitute the model parameters $\theta = (w_{ij}, a_i, b_j)$, and the normalization factor

$$Z_\theta := \sum_{x, h} e^{-E_\theta(x, h)} \quad (2)$$

is referred to as the *partition function*. The model distribution $\hat{p}_\theta(x)$ that approximates the target $p(x)$ is obtained from marginalization over the hidden units, $\hat{p}_\theta(x) := \sum_h \hat{p}_\theta(x, h)$.

The major drawback of RBMs is that the computational cost to evaluate Z_θ (and hence $\hat{p}_\theta(x, h)$ and $\hat{p}_\theta(x)$) scales exponentially with $\min\{M, N\}$ (see also Methods), which renders the model intractable in practice [25]. Therefore, both training (i.e., finding the optimal θ) and deployment (i.e., applying a trained model) rely on approximate sampling from $\hat{p}_\theta(x)$, typically via Markov chains. Ideally, one wishes to generate samples both *efficiently*, in the sense of minimal correlation and computational cost, and *accurately* in the sense of a faithful representation of the target $p(x)$. Unfortunately, these two goals generally compete and cannot be achieved simultaneously.

In this work, we explore the tradeoff relationship between accuracy and efficiency by identifying three distinct regimes of RBM training as illustrated in Fig. 1: (i) independent learning, where the accuracy can be improved without sacrificing efficiency; (ii) correlation learning, where higher accuracy entails lower efficiency, typically in the form of a power-law tradeoff; and (iii) degradation, where limited expressivity, overfitting, and/or approximations in the learning algorithm lead to reduced efficiency with no gain or even loss of accuracy.

Biased or inefficient sampling is a known limitation of standard training algorithms [4, 26], but it is not an artifact of deficient training methods. Rather, it should be understood as an intrinsic limitation of the RBM model. Yet its consequences for the usefulness of trained models in applications have received relatively little attention thus far. Our observations (i)–(iii) above elucidate the inner workings of RBMs and imply that, depending on the intended applications, aiming at maximal accuracy may not always be beneficial. We demonstrate the various aspects of these findings by way of several prob-

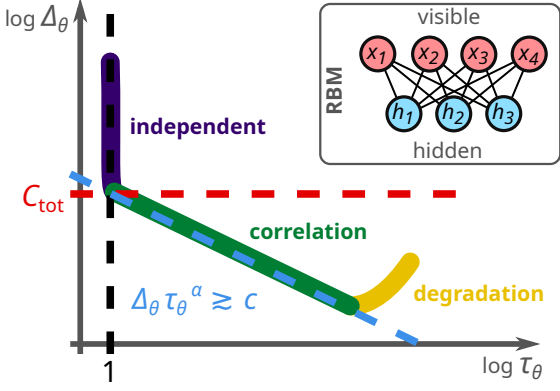


FIG. 1. Schematic illustration of the three learning regimes of Restricted Boltzmann Machines (RBMs), characterized by the relationship between the model’s divergence Δ_θ from the target distribution (accuracy, cf. Eq. (3)) and its integrated autocorrelation time τ_θ (efficiency, cf. Eq. (6)): independent learning with improved accuracy at no efficiency loss, correlation learning with a power-law tradeoff relation between accuracy and efficiency, and the degradation regime with steady or diminishing accuracy and loss of efficiency. Inset: Schematic illustration of the RBM structure comprised of visible and hidden units.

lems, ranging from quantum-state tomography for the transverse-field Ising chain (TFIC, cf. Fig. 2) to pattern recognition and image generation (Figs. 3 and 4); see also the figure captions and Methods for more details on the examples.

RESULTS

Accuracy and efficiency

A natural measure for the accuracy of the model distribution $\hat{p}_\theta(x)$ is its Kullback-Leibler (KL) divergence $D_{\text{KL}}(p||\hat{p}_\theta)$ [27] with respect to the target distribution $p(x)$,

$$\Delta_\theta := D_{\text{KL}}(p||\hat{p}_\theta) \equiv \sum_x p(x) \log \frac{p(x)}{\hat{p}_\theta(x)}, \quad (3)$$

which is nonnegative and vanishes if and only if the distributions $p(x)$ and $\hat{p}_\theta(x)$ agree. Indeed, Δ_θ provides the basis of most standard training algorithms for RBMs such as contrastive divergence (CD) [1, 2], persistent CD (PCD) [3], fast PCD [30], or parallel tempering [26, 31]. Adopting a gradient-descent scheme with Δ_θ as the loss function, one would ideally update the parameters according to

$$\theta_k(t+1) - \theta_k(t) = -\eta \left[\left\langle \frac{\partial E_\theta(x, h)}{\partial \theta_k} \right\rangle_{\hat{p}_\theta(h|x)p(x)} - \left\langle \frac{\partial E_\theta(x, h)}{\partial \theta_k} \right\rangle_{\hat{p}_\theta(x, h)} \right], \quad (4)$$

where $\eta > 0$ is the learning rate and $\hat{p}_\theta(h|x)$ is the conditional distribution of the hidden units given the visible ones. Since the latter distribution factorizes and the dependence on Z_θ cancels out (see Methods for explicit expressions), the first average on the right-hand side of (4) can readily be evaluated. More precisely, since $p(x)$ is unknown, it needs to be approximated by the empirical distribution $\tilde{p}(x; S) := \frac{1}{|S|} \sum_{\tilde{x} \in S} \delta_{x, \tilde{x}}$ for a (multi)set of *training data* $S := \{\tilde{x}^{(1)}, \dots, \tilde{x}^{(|S|)}\}$, which are assumed to be independent samples drawn from $p(x)$. Hence the effective loss function is $\tilde{\Delta}_\theta^{(S)} := \sum_x \tilde{p}(x; S) \log \frac{\tilde{p}(x; S)}{\hat{p}_\theta(x)}$, which is an empirical counterpart of (3).

The second average in (4), however, involves the full model distribution (1) and is thus not directly accessible in practice. Instead, it is usually approximated by sampling alternately from the accessible conditional distributions $\hat{p}_\theta(h|x)$ and $\hat{p}_\theta(x|h)$, leading to a Markov chain of the form

$$x^{(0)} \rightarrow h^{(0)} \rightarrow x^{(1)} \rightarrow h^{(1)} \rightarrow \dots \quad (5)$$

The distribution of $(x^{(n)}, h^{(n)})$ converges to the model distribution $\hat{p}_\theta(x, h)$ as $n \rightarrow \infty$. Truncating the chain (5) at a finite $n = n_{\text{CD}}$, we obtain a (biased) sample from that distribution, whose bias vanishes as $n_{\text{CD}} \rightarrow \infty$ [32], but depends on the initialization of the chain for finite n_{CD} . In our numerical examples, we will usually adopt the common CD algorithm, which chooses $x^{(0)}$ as a sample from the training data S , or the PCD algorithm, where $x^{(0)}$ is a sample from the chain of the previous update step (see also Supplementary Note 1). Subsequently, the Markov chain (5) can be used to generate a new, but correlated sample. Similarly, when analyzing and deploying a model $\hat{p}_\theta(x)$ after training, new samples are typically generated by means of Markov chains (5), with the caveat that those samples are correlated and thus not independent.

To quantify the *sampling efficiency*, we therefore consider the integrated autocorrelation time [33]

$$\tau_\theta := 1 + 2 \sum_{n=1}^{\infty} \frac{g_\theta(n)}{g_\theta(0)}, \quad (6)$$

where $g_\theta(n) := \frac{1}{M} \sum_i [\langle x_i^{(0)} x_i^{(n)} \rangle - \langle x_i^{(0)} \rangle^2]$ is the mean correlation function of the visible units for the Markov chain (5) in the stationary regime, i.e., $x^{(0)} \sim \hat{p}_\theta(x)$. Notably, τ_θ is independent of the training algorithm since it depends only on the RBM parameters θ , but not on the different initialization schemes of the Markov chains in (P)CD and its variants. In practice, particularly when utilizing the scheme (5) to employ a trained model productively, one will start from an arbitrary distribution and discard a number of initial samples (ideally on the order of the mixing time [32, 34, 35]) to thermalize the chain and approach the stationary distribution $\hat{p}_\theta(x)$.

The interpretation of τ_θ as a measure of sampling efficiency is as follows: Suppose we have a number R of *independent* samples from the model distribution $\hat{p}_\theta(x)$

to estimate $\langle x_i \rangle$ (or $\frac{1}{M} \sum_i \langle x_i \rangle$). To obtain an estimate of the same quality via Gibbs sampling according to (5), we would then need on the order of $\tau_\theta R$ correlated Markov-chain samples (see, for example, Sec. 2 of Ref. [33] and also Methods). Hence the (minimal) value of $\tau_\theta = 1$ hints at independent (uncorrelated) samples, and the larger τ_θ becomes, the more samples are needed in principle, rendering the approach less efficient.

Note that the integrated autocorrelation time τ_θ defined in Eq. (6) is conceptually related to, but different from the mixing time of the Markov chain (see also Discussion below). Furthermore, different observables (i.e., functions of the visible units x_i) generally exhibit different autocorrelation times. As explained in detail in Methods, the quantity τ_θ from (6) is a weighted average of the autocorrelation times associated with the observables' elementary variables, namely the individual x_i . Hence we expect τ_θ to capture the relevant correlations and thus the sampling efficiency in the generic case. The evaluation of other correlation measures below will reinforce this notion. In addition, a quantitative comparison of autocorrelation times for different observables is provided in Supplementary Note 4 for the examples from Figs. 2 and 4a–c.

Our principal object of study is the mutual dependence of Δ_θ and τ_θ on the parameters θ for a given target distribution $p(x)$. As outlined above and illustrated in Fig. 1, there are three regimes the machine undergoes during the learning process. Globally, the overall tradeoff between accuracy and efficiency is numerically found to be bounded by a power law of the form

$$\Delta_\theta \tau_\theta^\alpha \gtrsim c, \quad (7)$$

where both c and the exponent α are positive constants whose meaning will be clarified in the following. Moreover, in the correlation-learning regime, Δ_θ and τ_θ are often directly related by a power law $\Delta_\theta \tau_\theta^{\alpha'} \simeq c'$, where the constants c' and α' are close to c and α , respectively.

Mechanism

With no specific knowledge about the target distribution, it is natural to initialize the RBM parameters $\theta = (\theta_k) = (w_{ij}, a_i, b_j)$ randomly. Moreover, the initial values should be sufficiently small so that any spurious correlations arising from the initialization are much smaller than the actual correlations in the target distribution and can be overcome within a few training steps. In the examples from Figs. 2–4, we draw the initial θ_k independently from a normal distribution $\mathcal{N}(\mu, \sigma)$ of mean μ and standard deviation σ , namely $w_{ij} \sim \mathcal{N}(0, 10^{-2})$ and $a_i, b_j \sim \mathcal{N}(0, 10^{-1})$ unless stated otherwise. A brief exploration of other initialization schemes, including Hinton's proposal [2] and examples with significant (spurious) correlations, can be found in Supplementary Note 3. In Figs. 2 and 3, the experiments were repeated for 5 independent runs for each hyperparameter configuration,

and the displayed data are averages over those runs at fixed training epoch t . No error bars are shown in these figures for clarity, but the spread of the point clouds typically serves as a decent visualization of the uncertainty. We also highlight that important information for the ensuing discussion is encoded in the coloring of the data points. Particularly, both the filling color and the border color convey correlation characteristics and hyperparameter dependencies as indicated in the legends and figure captions.

We now sketch how the three learning regimes and the tradeoff relation arise. Intuitively, the origin of the accuracy–efficiency tradeoff can be understood as follows: To improve the model representation $\hat{p}_\theta(x)$ of the target distribution $p(x)$, correlations of $p(x)$ between the different visible units x_i have to be incorporated into $\hat{p}_\theta(x)$. Since correlations between visible units are mediated by the hidden units in the RBM model (1), this inevitably increases the correlation between subsequent samples in the Markov chain (5) and thus leads to larger autocorrelation times τ_θ in (6). Nevertheless, the detailed relationship between Δ_θ and τ_θ and its remarkable structural universality turn out to be more subtle as discussed in the following.

In the *independent-learning regime*, which constitutes, the first stage of the natural learning dynamics, the loss Δ_θ is actually reduced without any significant increase of the autocorrelation time τ_θ . Hence the RBM picks up aspects of the target distribution whilst preserving independence of its visible units. The minimal loss Δ_θ that can be achieved with a product distribution of independent units x_i is given by the *total correlation* [36]

$$C_{\text{tot}}(p) := \sum_x p(x) \log \frac{p(x)}{p_1(x_1) \cdots p_M(x_M)} \quad (8)$$

of the target distribution. This quantity is thus the KL divergence (cf. Eq. (3)) from the product of marginal distributions $p_i(x_i)$ to the joint distribution $p(x) = p(x_1, \dots, x_M)$. It can be understood as a multivariate analog of mutual information. For an arbitrary product distribution $\hat{p}(x) := \prod_i \hat{p}_i(x_i)$, we have $D_{\text{KL}}(p||\hat{p}) = C_{\text{tot}}(p) + \sum_i D_{\text{KL}}(p_i||\hat{p}_i) \geq C_{\text{tot}}(p)$ (see Supplementary Note 5). Hence $C_{\text{tot}}(p)$ indeed lower-bounds the loss Δ_θ for independent units.

The value of $C_{\text{tot}}(p)$ is indicated by the red dashed lines in Figs. 1–4, and indeed marks the end of the independent-learning regime as defined by $\tau_\theta \simeq 1$ in Figs. 2–4. As a consequence, we can identify the constant c from the tradeoff relation (7), which bounds Δ_θ from below at $\tau_\theta = 1$ (see also Methods), with the total correlation $C_{\text{tot}}(p)$ of the target distribution, $c \simeq C_{\text{tot}}(p)$, as illustrated by the intersection of the red ($\Delta_\theta = C_{\text{tot}}(p)$), blue ($\Delta_\theta = c \tau_\theta^{-\alpha}$), and black ($\tau_\theta = 1$) dashed lines in Figs. 1–4.

A closer inspection of the total correlation $C_{\text{tot}}(\hat{p}_\theta)$ of the *model* distribution, encoded by the color gradients in Figs. 2–3, confirms that no significant correlations between the RBM's visible units build up as long as $\tau_\theta \simeq 1$,

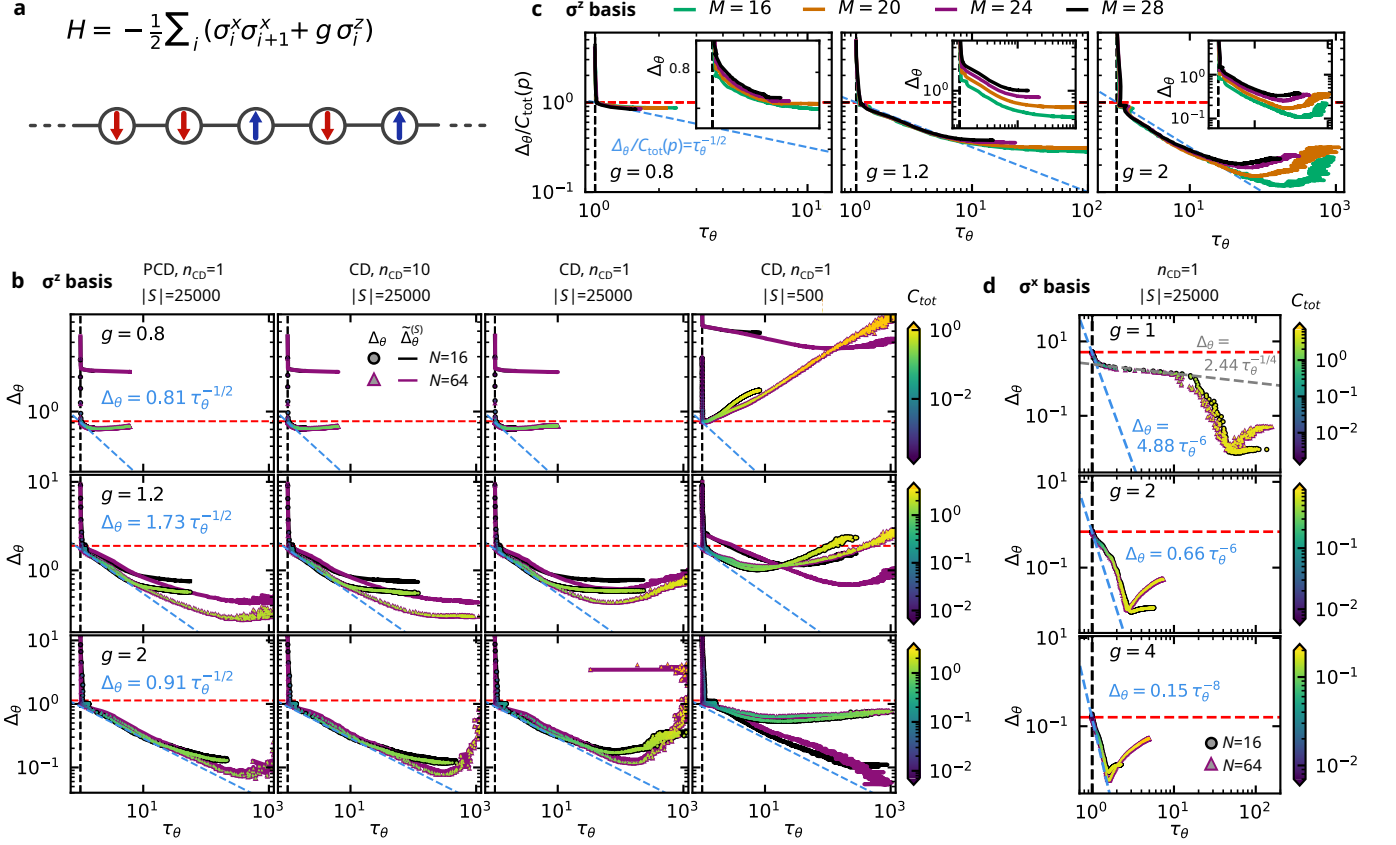


FIG. 2. RBM learning characteristics for a quantum state tomography task. The ground state of the transverse-field Ising chain with M lattice sites is reconstructed from magnetization measurements along a fixed axis, namely the z direction in (b, c) and the x direction in (d). Thus the ground state is represented in the eigenbases of the σ_i^z or σ_i^x Pauli operators associated with each lattice site. Training used contrastive divergence (CD) or persistent CD (PCD) with $\eta = 10^{-3}$, $B = 100$. (a) Hamiltonian and sketch of the transverse-field Ising chain, whose ground-state wave function $\psi(x)$ is the square root of the target distribution $p(x)$. (b) Exact loss Δ_θ (points) and empirical loss $\tilde{\Delta}_\theta^{(S)}$ (solid lines) vs. autocorrelation time τ_θ defined in (6), utilizing PCD (first column) or CD (last three columns), $n_{CD} = 10$ (second column) or $n_{CD} = 1$ (all other columns) and $|S| = 25000$ (first three columns) or $|S| = 500$ (fourth column) training samples, measured in the σ^z basis, for several different values of the magnetic field g (see left panel of each row). Markers: Δ_θ calculated from (3) with the filling color indicating the total correlation $C_{tot}(\hat{p}_\theta)$ of the model distribution (see right colorbars), and the border color and marker type indicating the number of hidden units N (see second panel in first row). Solid lines: $\tilde{\Delta}_\theta^{(S)}$ (see below Eq. (4)), sometimes masked under the Δ_θ data and thus not visible. Dashed lines: $\tau_\theta = 1$ (black), $\Delta_\theta = C_{tot}(p)$ (red), $\Delta_\theta = c\tau_\theta^{-\alpha}$ (blue). (c) $\Delta_\theta/C_{tot}(p)$ vs. τ_θ for various system sizes M utilizing CD with $n_{CD} = 1$, $N = 16$, $|S| = 25000$, σ^z basis, and g as indicated in each panel. As a result of rescaling the loss Δ_θ with the total correlation $C_{tot}(p)$ of the target distribution, the learning curves collapse in the independent- and correlation-learning regimes. Inset: Same data, but without the rescaling. (d) Δ_θ vs. τ_θ for CD training in the σ^x basis, with $|S| = 25000$ samples and $n_{CD} = 1$. Markers and dashed lines as in (b). All curves correspond to averages over 5 independent training runs.

providing further justification for labeling this stage as the “independent-learning” regime. The time spent in this regime can be reduced by adjusting the biases a_i to the activation frequencies of the visible units in the training data as suggested by Hinton [2] (see also Supplementary Note 3).

The independent-learning regime is thus characterized by $\tau_\theta \simeq 1$ and $\Delta_\theta \gtrsim C_{tot}(p)$. As soon as Δ_θ falls below $C_{tot}(p)$, the RBM enters the *correlation-learning regime* and starts to exhibit noticeable dependencies between its visible units, accompanied by an increase of τ_θ . This regime is characterized by $\Delta_\theta \lesssim C_{tot}(p)$ and $\frac{\partial\tau_\theta}{\partial\Delta_\theta} < 0$,

meaning that τ_θ grows as Δ_θ decreases. Quantitatively (cf. Figs. 2b–d, 3b,e, 4b,c), we find that the functional dependence between Δ_θ and τ_θ is (piecewise) power-law-like and often closely follows the lower bound provided by the tradeoff relation (7).

In most of our examples, the exponent α turns out to be well approximated by $\alpha \simeq \frac{1}{2}$. The notable exception is the example in Fig. 2d of TFIC ground-state tomography in the σ^x basis (but not the σ^z basis; see figure caption for details), where a value of $\alpha \approx 6 \dots 8$ seems more appropriate. Roughly speaking, α quantifies how efficiently the prevailing correlations in the target distribution $p(x)$

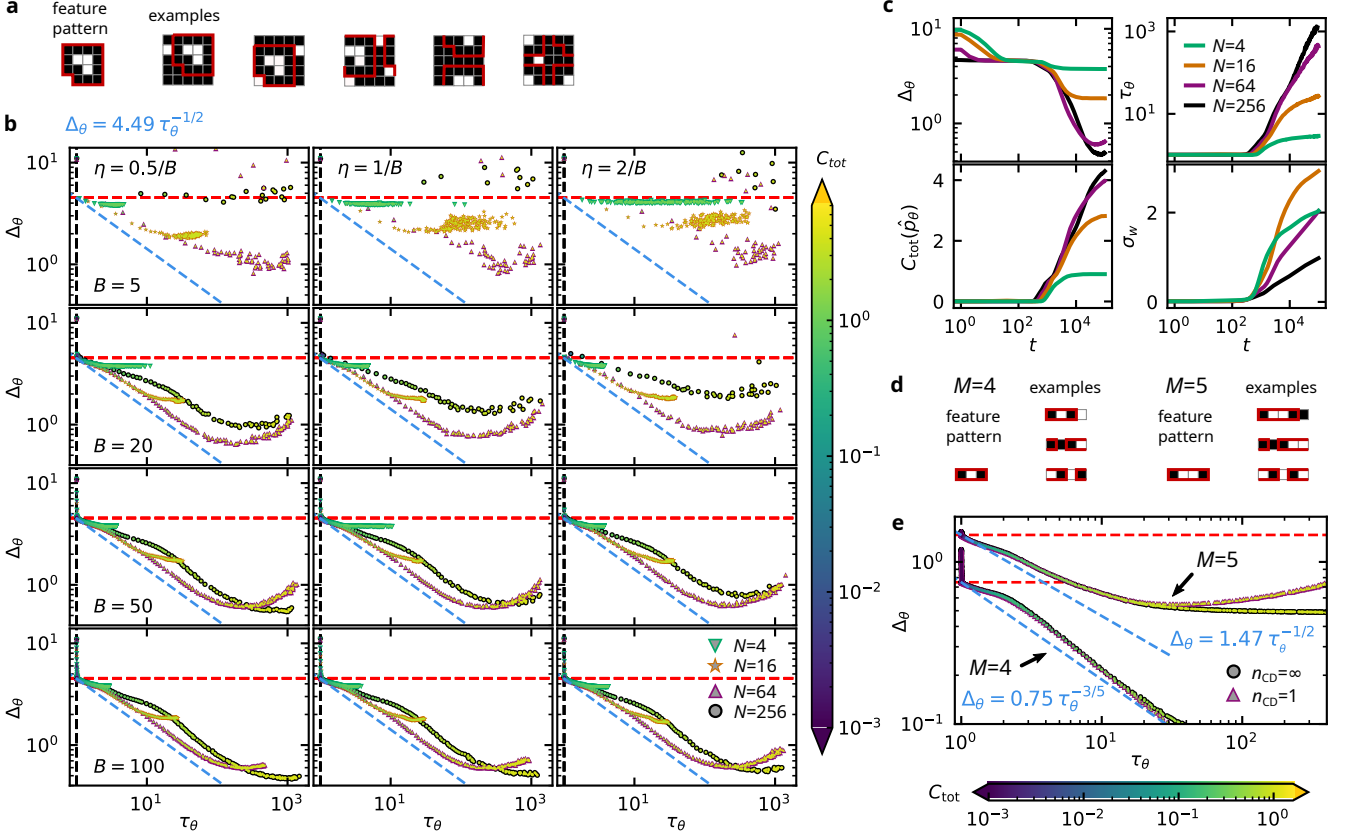


FIG. 3. RBM learning characteristics for a pattern recognition task. (a) The target distribution consists of $M = 5 \times 5$ “images” with periodic boundary conditions and a fixed 15-pixel “hook” pattern implanted at random locations, where the remaining pixels are active (white) with probability $q = 0.1$. (b) Exact loss Δ_θ vs. autocorrelation time τ_θ for RBMs with different numbers of hidden units N (see legend), trained on the distribution from (a) using contrastive divergence of order $n_{\text{CD}} = 1$ with $|S| = 5000$ training samples and various values of the batch size B (rows) and learning rate η (columns). Data points are averages over 5 independent runs. (c) Δ_θ , τ_θ , total correlation $C_{\text{tot}}(\hat{p}_\theta)$ of the model distribution, and the standard deviation of the weights $\sigma_w := (\frac{1}{MN-1} \sum_{i,j} w_{ij}^2)^{1/2}$ as a function of the training epoch t for various N ; $\eta = 0.005$, $B = 100$ (cf. bottom left panel of (b)). (d) Simplified model of $M = 1 \times 4$ or $M = 1 \times 5$ images with an implanted “black-white(-white)-black” pattern. (e) Δ_θ vs. τ_θ for RBMs with $N = 2$ hidden units trained on the distributions from (d) using the full target distribution (i.e., $|S| = \infty$) and exact continuous-time gradient descent with either the full model distribution $\hat{p}_\theta(x, h)$ ($n_{\text{CD}} = \infty$) or contrastive divergence of order $n_{\text{CD}} = 1$. Data points are averages over 100 independent runs with different initial conditions. In (b) and (e), fill colors indicate the total correlation $C_{\text{tot}}(\hat{p}_\theta)$ of the model distribution (see colorbars), border colors and marker types indicate the number of hidden units N (see legends in bottom-right corners).

can be encoded in the RBM model $\hat{p}_\theta(x)$. A larger value of α implies that the tradeoff (7) is less severe, indicating a closer structural similarity of $p(x)$ to the model family $\hat{p}_\theta(x)$.

The relationship between accuracy and efficiency in the correlation-learning regime turns out to be remarkably stable against variations of the architecture or the training details, suggesting that it is indeed an intrinsic limitation of the RBM model whose qualitative details are essentially determined by the target distribution. First, as long as training is stable, the Δ_θ - τ_θ learning trajectories are almost independent of further hyperparameters such as the number of training samples $|S|$, the mini-batch size B , or the learning rate η . This is illustrated in Fig. 3b (see Supplementary Note 5 for further examples), which also visualizes how training becomes unsta-

ble if η or B become too small, leading to underperforming machines with $(\tau_\theta, \Delta_\theta)$ further away from the global bound (7). Second, changing the approximation of the model averages in (4) does not affect the relation between Δ_θ and τ_θ . In fact, approximation schemes which achieve a smaller loss Δ_θ increase the autocorrelation time τ_θ in accordance with the tradeoff (7). This is exemplified by variations in the order (n_{CD}) and the initialization (CD vs. PCD) of the training chains (5) in Fig. 2b. Third, as long as the loss is sufficiently above the expressivity threshold (see below), the relationship between Δ_θ and τ_θ is largely insensitive to the number of hidden units N (see Figs. 2b,d, 3b, 4b,c). Fourth, the learning characteristics appear to be intrinsic to the problem *type*, but not its *size* if a natural scaling for the number of visible units M exists. To this end, we consider the TFIC ex-

ample and vary the number of lattice sites M in Fig. 2c. While this changes the total correlation $C_{\text{tot}}(p)$ of the target distribution, the rescaled curves of $\Delta_\theta/C_{\text{tot}}(p)$ vs. τ_θ collapse almost perfectly onto a single universal curve in the independent- and correlation-learning regimes.

The end of the correlation-learning regime and the crossover into the *degradation regime* is influenced by various (hyper)parameters. An absolute limit for the minimal value of Δ_θ results from the class of distributions that can be represented by the RBM. This “expressivity” is controlled by the number of hidden units N . For sufficiently large N , the RBM model can approximate any target distribution with arbitrary accuracy [5, 37–39]; hence there is no absolute minimum for Δ_θ in principle. In practice, however, the number of hidden units is limited by the available computational resources. Note that the scaling of this expressivity threshold is analyzed in some detail in Ref. [40] for the TFIC example (cf. Fig. 2).

Ceasing accuracy improvement due to limited expressivity is exemplified by Fig. 3b in the stable regime ($B \gtrsim 50$), where we note that the achievable minimal loss decreases significantly from $N = 4$ to 16 to 64 (the same behavior can also be observed in Fig. 4b,c). Employing even more hidden units, however, does not facilitate any significant gain in accuracy, and the learning characteristics for $N = 256$ in Fig. 3b actually signal slightly worse performance in terms of the accuracy–efficiency tradeoff, i.e., a larger offset from the global lower bound (blue dashed line).

If N is sufficiently large, the approximations leading to a bias of the (exact) update step (4) will usually take over eventually and lead into the degradation regime even if the expressivity threshold has not yet been reached.

The first of those approximations is use of the empirical distribution $\tilde{p}(x; S)$ in lieu of the unknown true target distribution $p(x)$. This may result in overfitting, a phenomenon common to many machine-learning approaches: The RBM may pick up finite-size artifacts of $\tilde{p}(x; S)$, particularly when the resolution of genuine features in the model distribution approaches the resolution of those features in the empirical distribution. Overfitting is the primary reason for degradation in the fourth column of Fig. 2b, where the size of the training dataset $|S|$ is rather small. Comparing the training error $\tilde{\Delta}_\theta^{(S)}$ (solid lines, see below (4)) with the test error Δ_θ (data points, see Eq. (3)), we observe that the former continues to decrease even though the latter actually increases.

In the first three columns of Fig. 2b, by contrast, $\tilde{\Delta}_\theta^{(S)}$ usually follows Δ_θ closely (thus the solid lines are often hidden behind the data points). Here, degradation is due to the second limiting approximation of the update step (4), namely the replacement of averages over the model distribution $\hat{p}_\theta(x, h)$ by Markov-chain samples (5). In fact, this is directly related to the definition of τ_θ because larger values imply that the chain (5) needs to be run for a longer time in order to obtain an effectively independent sample (see below Eq. (6)). Indeed, smaller

losses can be achieved for larger n_{CD} (second vs. third column). Similarly, at fixed n_{CD} , PCD can reach higher accuracies than CD (first vs. third column; see also Supplementary Note 5).

Finally, we turn to the smallest example from Fig. 3d–e. In this case, we can directly integrate the continuous-time ($\eta = 0$) update equations (4) with the full target distribution $p(x)$ (i.e., $|S| = \infty$) and the exact model distribution $\hat{p}_\theta(x, h)$ (i.e., $n_{\text{CD}} = \infty$) for RBMs with $N = 2$ hidden units (see also Supplementary Note 1). We again observe a power-law tradeoff between Δ_θ and τ_θ with $\alpha \simeq \frac{1}{3} \dots \frac{3}{5}$, limited by the machine’s expressivity in the $M = 5$, but not in the $M = 4$ case. Moreover, by averaging over $\hat{p}_\theta^{(1)}(x, h) := \hat{p}_\theta(h|x) \sum_{x', h'} \hat{p}_\theta(x|h') \hat{p}_\theta(h'|x') p(x')$ instead of $\hat{p}_\theta(x, h)$ in (4), we can adopt the exact CD update of order $n_{\text{CD}} = 1$. This reintroduces the correlation bias into the updates and indeed leads to stronger deviations from the power-law behavior for $M = 5$, with increasing Δ_θ in the degradation regime.

Towards applications

All examples discussed so far (Figs. 2, 3 and 4a–c) involved only a small number of visible units M so that the accuracy measure Δ_θ could be evaluated numerically exactly. In practice, this is impossible because neither the target distribution $p(x)$ nor the model distribution $\hat{p}_\theta(x)$ are directly accessible. In the following, we will sketch how learning characteristics and the accuracy–efficiency tradeoff can be analyzed approximately in applications and apply the ideas, in particular, to the MNIST dataset [8] as a standard machine-learning benchmark of larger problem size (see Fig. 4d,e).

To approximate the accuracy measure Δ_θ , the target distribution $p(x)$ is usually replaced by the empirical distribution $\tilde{p}(x; T)$ for a (multi)set of test samples T (independent of the training samples S). If both M and N become large, $\hat{p}_\theta(x)$ must be approximated by an empirical counterpart as well. To this end, a collection of independent samples from $\hat{p}_\theta(x)$ is needed. Typically, it will be generated approximately by Markov chains (5), which directly leads back to the autocorrelation time τ_θ from (6) as a measure for the number of steps required in (5) to obtain an effectively independent sample.

Estimating τ_θ , in turn, should remain feasible along the lines outlined in Methods even if M and N are large. To be precise, if it turns out to be impossible in practice to reliably estimate τ_θ , then any conclusions about the model distribution $\hat{p}_\theta(x)$ drawn from Markov chains like (5) are equally unreliable. In other words, if τ_θ (or, more generally, the integrated autocorrelation time of the observable of interest) cannot be computed, the trained model itself becomes useless as a statistical model of the target distribution. A particular challenge are metastabilities where the chains spend large amounts of time in a local regime of the configuration space and only rarely transition between those regimes. These can be caused,

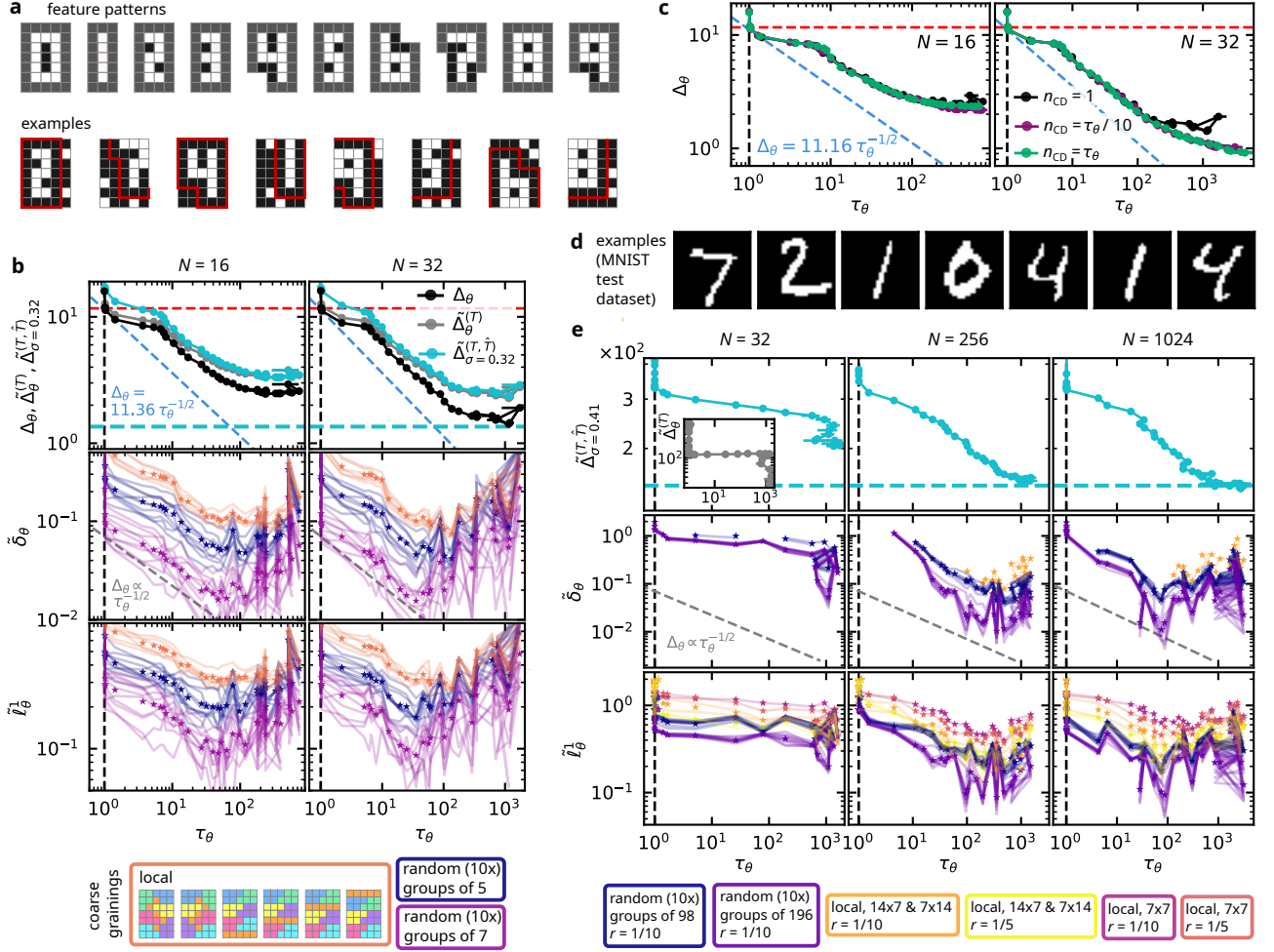


FIG. 4. Approximate RBM learning characteristics on digit images. (a) Images of $M = 5 \times 7$ pixels showing patterns of the digits 0 through 9 (selected uniformly) at a random location. Gray pixels must either be made black ($x_i = 0$) or be cut away by the image boundaries (see examples in the second row). Pixels that are not part of the pattern are active (white) with probability $q = 0.1$. The total number of such images is 40 507 353. (b) Various loss measures vs. autocorrelation time τ_θ for $N = 16$ (left) and $N = 32$ (right) hidden units, utilizing persistent contrastive divergence (PCD) with $n_{CD} = 1$, $\eta = 0.005$, $B = 100$ on $|S| = 50\,000$ training images. Top: Exact loss Δ_θ (black), exact test error $\tilde{\Delta}_\theta^{(T)}$ (empirical loss for a test dataset T of $|T| = 10\,000$ images, gray), and Gaussian-smoothed empirical loss estimate $\tilde{\Delta}_\sigma^{(T, \hat{T})}$ ($|\hat{T}| = 10^6$, $\sigma = 0.32$, cyan). The cyan dashed line marks $\tilde{\Delta}_{\sigma=0.32}^{(T,S)} = 1.354$, the minimal Gaussian-smoothed loss estimate between the test and training datasets. Middle: Empirical error $\tilde{\delta}_\theta$ using majority-rule ($r = 1$) coarse-grainings of samples from the target and model distributions, partitioning pixels into local or random groups (see main text for details). Solid lines: results for individual partitions; star markers: average of the solid lines of the same partitioning type (color, see legend). Bottom: empirical error $\tilde{\ell}_\theta$ for the same coarse-grainings. (c) Δ_θ vs. τ_θ for $N = 16$ (left) and $N = 32$ (right) hidden units, utilizing persistent contrastive divergence (PCD) with fixed ($n_{CD} = 1$) or adaptive ($n_{CD} \propto \tau_\theta$) approximation order; other hyperparameters as in (b). (d) Examples from the MNIST dataset, which comprises images of $M = 28 \times 28$ pixels showing handwritten digits. (e) Similar to (b), but for the MNIST dataset and PCD training with $n_{CD} = 1$, $\eta = 10^{-4}$, $B = 100$, $|S| = 60\,000$, $|T| = 10\,000$, $|\hat{T}| = 10^6$, $\sigma = 0.41$, and $\tilde{\Delta}_{\sigma=0.41}^{(T,S)} = 147.4$. Missing data points correspond to $\tilde{\delta}_\theta = \infty$ and/or unreliable τ_θ estimates.

for instance, by a multimodal structure of the target distribution. If undetected, those metastabilities can lead to vastly underestimated autocorrelation times.

Once a set of (approximately) independent samples \hat{T} from $\hat{p}_\theta(x)$ is available, the KL divergence $D_{KL}(\hat{p}(\cdot; T) || \hat{p}(\cdot; \hat{T}))$ can serve as a proxy for Δ_θ in principle. In practice, however, this approach will not be

viable because this proxy diverges whenever there is a sample \tilde{x} in T which is not found in \hat{T} , meaning that the sample size required for \hat{T} will often be out of reach.

We suggest two alternative approaches to mitigate this problem. First, we consider smoothing the empirical model distribution $\tilde{p}(x; \hat{T})$ by convolving it with a Gaussian kernel $k(x; \mu, \sigma) := N_\sigma^{-1} e^{-(x-\mu)^2/2\sigma^2}$,

where $N_\sigma := \sum_{d=0}^M \binom{M}{d} e^{-d/2\sigma^2}$, leading to $\tilde{p}_\sigma(x; \hat{T}) := \frac{1}{|\hat{T}|} \sum_{\hat{x} \in \hat{T}} k(x; \hat{x}, \sigma)$. The KL divergence $\tilde{\Delta}_\sigma^{(T, \hat{T})} := D_{\text{KL}}(\tilde{p}(\cdot; T) \parallel \tilde{p}_\sigma(\cdot; \hat{T}))$ then approximates Δ_θ , where σ is chosen so as to make $\tilde{\Delta}_\sigma^{(T, S)}$ minimal, i.e., when using the training data S as the empirical model distribution [26] (see also Supplementary Note 2). As shown in the first row of Fig. 4b, $\tilde{\Delta}_\sigma^{(T, \hat{T})}$ reproduces essentially the same behavior as Δ_θ and $\tilde{\Delta}_\theta^{(T)}$.

Second, we propose coarse-graining the samples in T and \hat{T} , such that every $\tilde{x} = (\tilde{x}_1, \dots, \tilde{x}_M) \in T, \hat{T}$ is mapped to a new configuration $\tilde{y} = (\tilde{y}_1, \dots, \tilde{y}_L)$ with $\tilde{y}_l \in \{0, 1\}$ and $L < M$. Denoting the resulting multisets of reduced configurations by T' and \hat{T}' , we then consider the KL divergence $\tilde{\delta}_\theta := D_{\text{KL}}(\tilde{p}(\cdot; T') \parallel \tilde{p}(\cdot; \hat{T}'))$ of the associated empirical distributions as a qualitative approximation of Δ_θ . To be specific, in Fig. 4, we employ a weighted majority rule for coarse graining using random or local partitions of the visible units into L subsets, such that $\tilde{y}_l = 1$ if a fraction of r or more units in the l th subset is active (see Methods for details).

While some of the quantitative details are inevitably lost as a result of the coarse graining, the results in Fig. 4b show that the accuracy measure $\tilde{\delta}_\theta$ still conveys similar learning characteristics as the exact loss Δ_θ . Remarkably, even the same exponent $\alpha \simeq \frac{1}{2}$ is found to describe the tradeoff between $\tilde{\delta}_\theta$ and τ_θ in the correlation-learning regime. On the other hand, the coarse-grained loss $\tilde{\delta}_\theta$ appears to deteriorate somewhat prematurely, especially for the random coarse grainings, indicating that late improvements of Δ_θ involve finer, presumably local correlations that cannot be captured by $\tilde{\delta}_\theta$ in these cases.

Furthermore, we also consider the L^1 distance $\tilde{\ell}_\theta^1 := \sum_x |\tilde{p}(x; T') - \tilde{p}(x; \hat{T}')|$ between the reduced empirical distributions as an accuracy measure. Its advantage is that—unlike $\tilde{\delta}_\theta$ —it does not suffer from divergences when $T' \not\subseteq \hat{T}'$ (cf. Fig. 4e in particular). As shown in Fig. 4b and e, the $\tilde{\ell}_\theta^1 - \tau_\theta$ curves qualitatively agree with their $\tilde{\delta}_\theta - \tau_\theta$ counterparts and can thus serve as a more stable way to monitor the tradeoff in case of smaller sample sizes.

Inspecting the learning characteristics in the MNIST example from Fig. 4e, we observe that the relationship between the accuracy measures $\tilde{\Delta}_\sigma^{(T, \hat{T})}$, $\tilde{\delta}_\theta$, $\tilde{\ell}_\theta^1$ and the efficiency measure τ_θ are qualitatively similar as in the simpler example in Fig. 4b, especially for the more expressive RBMs with $N \geq 256$. Notably, we find an initial regime with decreasing $\tilde{\Delta}_\sigma^{(T, \hat{T})}$ and $\tilde{\ell}_\theta^1$ at $\tau_\theta = 1$ ($\tilde{\delta}_\theta = \infty$ here due to the aforementioned undersampling problem), followed by an approximately power-law-like tradeoff between accuracy and efficiency, and finally ceasing improvement ($\tilde{\Delta}_\sigma^{(T, \hat{T})}$) or deterioration ($\tilde{\delta}_\theta$, $\tilde{\ell}_\theta^1$) at increasing τ_θ . For $N = 32$, by contrast, the RBM accuracy does not improve much beyond the independent-learning threshold, except for somewhat unstable fluctuations at very late training stages. Hence we expect that the same tradeoff mechanism identified in the small-scale examples from

Figs. 2 through 4a–c also governs the behavior of more realistic, large-scale learning problems.

Altogether, our present results suggest a couple of approaches to monitor the accuracy and efficiency in applications with large input dimension M . First, we propose estimating the autocorrelation time τ_θ at selected epochs during training and stop when it exceeds the threshold set by the available evaluation resources in the intended use case. Second, it may be helpful to train RBMs with smaller numbers of hidden units N so that the test error $\tilde{\Delta}_\theta^{(T)}$ can be evaluated exactly (see also Methods), even though those small- N machines will typically not reach the desired accuracies. Since the onset of the correlation-learning regime and the subsequent initial progression are essentially independent of N , the relationship between $\tilde{\Delta}_\theta^{(T)}$ and τ_θ for small N can provide an intuition and perhaps even a cautious extrapolation of the behavior for larger N . Third, empirical accuracy measures such as $\tilde{\Delta}_\theta^{(T, \hat{T})}$, $\tilde{\delta}_\theta$ and $\tilde{\ell}_\theta^1$ can assure that the machine is still learning and possibly even map out the beginning of the degradation regime. Fourth, estimates of τ_θ can be naturally obtained *en passant* when using the PCD algorithm. These estimates can then be employed to adapt the length n_{CD} of the Markov chains (5) to the current level of correlations when approximating the model averages in (4). While we leave a detailed analysis of the resulting “adaptive PCD” algorithm for future work, preliminary results (see Fig. 4c) suggest that one can indeed reach better accuracies this way, while the tradeoff (7) remains valid.

DISCUSSION

In summary, the accuracy–efficiency tradeoff is an inherent limitation of the RBM architecture and its reliance on Gibbs sampling (5) to assess the model distribution $\hat{p}_\theta(x)$. Depending on the eventual application of the trained model, this limitation should already be taken into account when planning and performing training: Aiming at higher accuracy implies that more resources will be required also in the production stage to evaluate and employ the trained model in an unbiased fashion.

Not least, the tradeoff directly affects the training process itself. It is well known that common training algorithms like contrastive divergence and its variants are biased [1, 42] and that the bias increases with the magnitude of the weights [32, 43]. Hence there exists an optimal stopping time for training at which the accuracy becomes maximal, but unfortunately, no simple criterion in terms of accessible quantities is known to determine this stopping time [43, 44]. Approximate test errors like $\tilde{\Delta}_\sigma^{(T, \hat{T})}$, $\tilde{\delta}_\theta$ or $\tilde{\ell}_\theta^1$ can provide a rough estimate for when deterioration sets in, but are insensitive to finer details by construction. By contrast, taking the reconstruction error as a measure for the model accuracy, which is still not

uncommon since it is easily accessible, is downright detrimental from a sampling-efficiency point of view because it decreases with increasing correlations between samples. Since it is not correlated with the actual loss either [43], the reconstruction error should rather be regarded as an efficiency measure (with larger “error” indicating higher efficiency).

The aforementioned fact that the magnitude of the weights is closely related to the autocorrelation time τ_θ (see also Supplementary Note 5) provides a dynamical understanding of the bias in the sense that larger τ_θ calls for more steps in the Markov chain (5) to obtain an effectively independent sample. Similar conclusions have been drawn from studies of the mixing time of RBM Gibbs samplers [32, 34, 35]. The mixing time quantifies how many steps in (5) are necessary to reach the stationary distribution $\hat{p}_\theta(x)$ from an arbitrary initial distribution for $x^{(0)}$. In CD training, where $x^{(0)}$ is taken from the training data (meaning that it is a sample drawn from $p(x)$ by assumption), it is particularly relevant for the early training stages when $\hat{p}_\theta(x)$ is possibly far away from the target. For analyzing a trained model, by contrast, the mixing time is less important because it only provides a constant offset to the sampling efficiency by quantifying the burn-in steps in (5), i.e., the number of samples to discard until the stationary regime is reached, whereafter one will start recording samples to actually assess $\hat{p}_\theta(x)$. Similarly, correlations in the PCD update steps are better described by autocorrelation times like τ_θ , at least if the learning rate is sufficiently small so that the Markov chains can be considered to operate in the stationary regime throughout training, and the same applies to ordinary CD updates at later training stages.

There are a variety of proposals to modify the sampling process so that correlations between subsequent samples in an appropriate analog of (5) are reduced, including the above-sketched PCD extension with τ_θ -adaptive order of the Markov-chain sampling (see also Fig. 4c), parallel tempering [26, 31], mode-assisted training [45], or occasional Metropolis-Hastings updates [46, 47]. However, these adaptations come with their own caveats and the extent to which correlations are reduced may depend strongly on the setting [34, 47]. Moreover, the computational complexity of these methods is usually higher because additional substeps are necessary to produce a new Markov-chain sample. While a detailed quantitative analysis is missing, the overall evaluation efficiency (e.g., the required computational resources) will presumably not be improved in general [25], and probably the only remedy to circumvent the sampling problem could be novel computing hardware such as neuromorphic chips [48–52], “memcomputing machines” [53], or quantum annealers [54, 55].

For a more comprehensive understanding of the trade-off mechanism, it would be desirable to elucidate the role of the exponent α in (7) and how it relates to properties of the target distribution $p(x)$. As discussed above, α roughly quantifies how apt the RBM architecture is to

represent $p(x)$, with larger values of α indicating better suitability. A related question is what distributions can be represented efficiently by RBMs in terms of the required number of hidden units [37, 39, 56]. Besides the number of “active” states, symmetries that make it possible to represent the correlations between various visible units with fewer hidden units could play an important role in affecting α (see also Supplementary Note 5). Furthermore, observing the marked transition from independent to correlation learning, one may naturally wonder whether there exists a hierarchy of how and when correlations are adopted during the correlation-learning regime [39, 57–60], particularly when α is ambiguous (e.g., in Fig. 2d; see also Supplementary Note 5). In any case, it is remarkable that in most of the examples we explored, α turns out to be approximately $\frac{1}{2}$, particularly at the initial stage of the correlation-learning regime. Whether this is a coincidence or a hint at some deeper universality principle is an intriguing open question.

METHODS

Conditional RBM distributions

The approach to use alternating Gibbs sampling of visible and hidden units via Markov chains of the form (5) is viable in practice only due to the bipartite structure of the RBM with direct coupling exclusively between one visible and one hidden unit. Consequently, the visible units are conditionally independent given the hidden ones and vice versa, e.g., $\hat{p}_\theta(h | x) = \prod_j \hat{p}_\theta(h_j | x)$ with

$$\hat{p}_\theta(h_j | x) = \frac{e^{(\sum_i w_{ij} x_i + b_j) h_j}}{1 + e^{\sum_i w_{ij} x_i + b_j}}, \quad (9)$$

and similarly $\hat{p}_\theta(x | h)$ can be obtained by replacing $x_i \leftrightarrow h_j$ and $a_i \leftrightarrow b_j$ and by summing over i in the exponents and taking the product over j . Sampling from $\hat{p}_\theta(h | x)$ and $\hat{p}_\theta(x | h)$ is thus of polynomial complexity in the number of units and can be carried out efficiently. Likewise, this explains why the first average on the right-hand side of (4) with $\tilde{p}(x; S)$ in lieu of $p(x)$ (sometimes called the “data average;” see also below Eq. (4)) can be readily evaluated. For $\theta_k = w_{ij}$, for example, one finds

$$\left\langle \frac{\partial E_\theta(x, h)}{\partial w_{ij}} \right\rangle_{\hat{p}_\theta(h | x) \tilde{p}(x; S)} = -\frac{1}{|S|} \sum_{x \in S} x_i \hat{p}_\theta(h_j = 1 | x), \quad (10)$$

and similarly for a_i and b_j .

The variability of samples obtained from those conditional distributions can be assessed in terms of their Shannon entropy, defined for an arbitrary probability distribution $p(x)$ as $S(p) := -\sum_x p(x) \log p(x)$. Specifi-

cally,

$$S(\hat{p}_\theta(h | x)) = \sum_j \left[\log \left(1 + e^{\sum_i w_{ij} x_i + b_j} \right) - \frac{\sum_i w_{ij} x_i + b_j}{1 + e^{-\sum_i w_{ij} x_i - b_j}} \right], \quad (11)$$

and, again, similarly for $\hat{p}_\theta(x | h)$. The entropy is maximal for the uniform distribution with $\theta_k = 0$ for all parameters. It remains large as long as the θ_k 's are small in magnitude and tends to decrease towards zero as $|\theta_k|$ increases unless there is a special fine-tuning for specific configurations h that leads to exact cancelations. Over multiple steps of the Markov chain (5), the samples will thus generically show more variability for small weights, whereas they develop stronger correlations as the weights grow [32, 43] (see also Supplementary Note 5).

Details on Δ_θ , $C_{\text{tot}}(\hat{p}_\theta)$ and related quantities

The measure of accuracy Δ_θ (exact loss, ideal test error) is calculated numerically exactly by carrying out the sums in Eqs. (2) and (3). Similarly, the total correlations $C_{\text{tot}}(p)$ of the target and model distributions are computed exactly according to (8) as a sum over all states that keeps track of the contributions from both the full distribution $p(x)$ and the marginal ones $p_i(x_i)$.

For the partition function (2), we can exploit the bipartite structure of the RBM's interaction graph, such that one of the sums can be factorized and thus be evaluated efficiently. For example, if $N \leq M$, we rewrite (2) as

$$Z_\theta = \sum_h e^{\sum_j b_j h_j} \prod_i \left(1 + e^{\sum_j w_{ij} h_j + a_i} \right), \quad (12)$$

and similarly if $M < N$. The sum over h in (12) involves 2^N terms, but the product over i in each summand consists of just M factors. Therefore, the computational complexity scales exponentially with $\min\{M, N\}$ only. For the sum in Eq. (3), we can exploit the sparsity of the target distribution $p(x)$ and restrict the (costly) evaluations of $\hat{p}_\theta(x)$ to those states with $p(x) > 0$. Notwithstanding, the system sizes for which the computation of Δ_θ remains viable is relatively small; see also Refs. [26, 43–45, 61] for studies of the exact RBM loss in small examples.

In practical applications, one does not have access to $p(x)$, but only to a collection of samples $S := \{\tilde{x}^{(1)}, \dots, \tilde{x}^{(|S|)}\}$ (training and/or test data). The empirical counterpart of Δ_θ for such a dataset S is

$$\tilde{\Delta}_\theta^{(S)} = -\frac{1}{|S|} \sum_{x \in S} \left[\sum_i a_i x_i + \sum_j \log \left(1 + e^{\sum_i w_{ij} x_i + b_j} \right) \right] + \log Z_\theta - \log |S|; \quad (13)$$

see also below Eq. (4). The critical part is again the partition function Z_θ . Due to the aforementioned factorization (cf. Eq. (12)), evaluating (13) remains feasible as long as the number of hidden units N is sufficiently small, even if M is large. Similarly, for small N , we can draw independent samples from $\hat{p}_\theta(x) = \sum_h \hat{p}_\theta(x | h) \hat{p}_\theta(h)$, without reverting to Markov chains and Gibbs sampling: We first generate independent samples $\{\tilde{h}^{(\mu)}\}$ of the hidden units, using the fact that $\hat{p}_\theta(h)$ remains accessible for small N . Subsequently, we sample configurations of the visible units using $\hat{p}_\theta(x | h = \tilde{h}^{(\mu)})$. This scheme was utilized to obtain the model test samples \hat{T} for the $N \leq 32$ examples in Fig. 4. For the examples with $N > 32$, the samples in \hat{T} were instead generated via Gibbs sampling according to (5), using 10 parallel chains and storing every τ_θ -th sample after 2×10^6 burn-in steps.

The accuracy measures $\tilde{\delta}_\theta$ and $\tilde{\ell}_\theta^1$ involve empirical distributions of coarse-grained visible-unit samples. These reduced samples are obtained by using a weighted majority rule: For a partition $\{L_1, \dots, L_L\}$ of the visible-unit indices $\{1, \dots, M\}$ and a threshold $r \in [0, 1]$, we define

$$f_\alpha(x) := \begin{cases} 1 & \text{if } \sum_{i \in L_\alpha} x_i \geq r |L_\alpha|; \\ 0 & \text{otherwise.} \end{cases} \quad (14)$$

For every sample \tilde{x} in a given multiset S , the associated coarse-grained sample is $\tilde{y} = (\tilde{y}_1, \dots, \tilde{y}_L)$ with $\tilde{y}_\alpha := f_\alpha(\tilde{x})$.

Details on τ_θ

To measure the efficiency of Gibbs sampling according to the Markov chain (5), we evaluate the integrated autocorrelation time τ_θ from (6). The general purpose of Gibbs sampling is to estimate the model average $\langle f(x) \rangle \equiv \langle f(x) \rangle_{\hat{p}_\theta(x)}$ of some observable $f(x)$, i.e., a function of the visible units. The sample mean $\bar{f} := \frac{1}{R} \sum_{n=0}^{R-1} f(x^{(n)})$ over a chain of R samples is an unbiased estimator of $\langle f(x) \rangle$ if the chain is initialized and thus remains in the stationary regime, $x^{(0)} \sim \hat{p}_\theta(x)$ (see also below Eq. (6)). The correlation function associated with $f(x)$ and the Markov chain (5) is

$$g_\theta^{(f)}(n) := \langle f(x^{(0)}) f(x^{(n)}) \rangle - \langle f(x) \rangle^2. \quad (15)$$

For any such correlation function $g_\theta^{(f)}(n)$, the corresponding integrated autocorrelation time is defined similarly to Eq. (6),

$$\tau_\theta^{(f)} := 1 + 2 \sum_{n=1}^{\infty} \frac{g_\theta^{(f)}(n)}{g_\theta^{(f)}(0)}. \quad (16)$$

To assess the reliability of the estimator \bar{f} , we inspect its variance

$$\langle \bar{f}^2 \rangle - \langle \bar{f} \rangle^2 = \frac{g_\theta^{(f)}(0)}{R} \left[1 + 2 \sum_{n=1}^{R-1} \left(1 - \frac{n}{R} \right) \frac{g_\theta^{(f)}(n)}{g_\theta^{(f)}(0)} \right]. \quad (17)$$

If the number of samples R is much larger than the decay scale of $g_\theta^{(f)}(n)$ with n (which is a prerequisite for estimating f reliably), the contribution proportional to $\frac{n}{R}$ becomes negligible in the sum and the term in brackets reduces to $\tau_\theta^{(f)}$ from (16); see also Sec. 2 of Ref. [33]. Observing that $g_\theta^{(f)}(0)$ is the variance of $f(x)$, the variance of the estimator \bar{f} from correlated Markov-chain samples is thus a factor of $\tau_\theta^{(f)}$ larger than the variance of the mean over independent samples. In other words, sampling via the Markov chain (5) requires $\tau_\theta^{(f)}$ more samples than independent sampling to reach the same standard error and is thus less efficient the larger τ_θ becomes.

In general, the integrated autocorrelation times $\tau_\theta^{(f)}$ can and will be different for different observables $f(x)$. The specific choice τ_θ from (6) is supposed to capture the generic behavior of typical observables. It focuses on the individual visible units x_i as the elementary building blocks. However, instead of taking the mean over the autocorrelation times $\tau_\theta^{(x_i)}$ for each unit $f(x) = x_i$, the averaging is performed at the level of the correlation functions $g_\theta^{(x_i)}(n)$; cf. below Eq. (6). The effect is a weighted average

$$\tau_\theta = \frac{\sum_i g_\theta^{(x_i)}(0) \tau_\theta^{(x_i)}}{\sum_i g_\theta^{(x_i)}(0)} \quad (18)$$

that gives higher importance to strongly fluctuating units with a large variance $g_\theta^{(x_i)}(0)$. This accounts for the fact that variability of the Markov-chain samples is more important for those units and reduces the risk of underestimating correlations when there are certain regions in the data that behave essentially deterministically, e.g., background pixels at the boundary of an image distribution.

In practice, if one is interested in a specific observable $f(x)$, the associated autocorrelation time $\tau_\theta^{(f)}$ should be monitored directly instead of (or along with) the generic τ_θ . While the quantitative details may differ, we expect that the scaling behavior and the tradeoff mechanism remain qualitatively the same. A comparison for different observables in the TFIC example from Fig. 2 and in the digit-pattern images from Fig. 4a–c can be found in Supplementary Note 4. We indeed observe that $\tau_\theta^{(f)}$ is usually largely proportional to τ_θ .

In our numerical experiments, we estimate τ_θ statistically from long Markov chains of the form (5) with n_{tot} samples. Due to sampling noise, the sum over time lags n in (6) must be truncated at a properly chosen threshold n_{max} to balance the bias and variance of the estimator. Following Ref. [33], we choose n_{max} as the smallest integer such that $n_{\text{max}} \geq \gamma \tilde{\tau}_\theta(n_{\text{max}})$, where γ is a constant and $\tilde{\tau}_\theta(n_{\text{max}})$ is the value obtained from truncating (6) at n_{max} using empirical averages to estimate the correlation function $g_\theta(n)$ (see below Eq. (6)) and exploiting translational invariance of the stationary state (i.e., $\langle x_i^{(0)} x_i^{(n)} \rangle = \langle x_i^{(k)} x_i^{(n+k)} \rangle$). If $g_\theta(n)$ follows an exponential decay, the bias of the estimator is of order $e^{-\gamma}$, and

we use $\gamma = 5$ in Figs. 2–3 and $\gamma = 8$ in Fig. 4. To reach the stationary regime, we initialize the chain (5) in a state sampled uniformly at random and thermalize it by discarding a large number of samples, at least on the order of $100\tau_\theta$, providing a reasonable buffer to account for mixing times that may exceed τ_θ (and would thus increase the bias if the number of discarded samples was too small).

In Fig. 4, we additionally maintain r_g independently initialized chains to estimate $g_\theta(n)$ and calculate τ_θ as described above, using the average over the r_g chains for $g_\theta(n)$. The estimates are considered to be reliable only if the variations between the means of the r_g chains are below 5%; otherwise the data points are discarded. Furthermore, we repeat the entire procedure r_τ times, leading to r_τ independent estimates of τ_θ . The error bars in Fig. 4 indicate the min-max spread between those r_τ estimates.

Power-law bound

In the examples from Figs. 2–4, the blue dashed lines indicate the power-law bound (7) for the accuracy–efficiency tradeoff. The constants c and α in this bound as stated in the respective figure panels were determined as follows: The exponent α is chosen to roughly match the average slope $-\frac{\partial \log \Delta_\theta}{\partial \log \tau_\theta}$ for the data points in the correlation-learning regime over all hyperparameter configurations $(n_{\text{CD}}, \eta, B, |S|)$ for any specific target distribution $p(x)$. If this choice is ambiguous (e.g., in Fig. 2d), the behavior in the beginning of the correlation-learning regime ($\tau_\theta \simeq 1, \Delta_\theta \simeq C_{\text{tot}}(p)$) is decisive. Once α is fixed, c is chosen as the maximum value such that $\Delta_\theta \tau_\theta^\alpha \geq c$ holds for all data points of all hyperparameter configurations simultaneously.

Examples

The first exemplary task (cf. Fig. 2) is quantum-state tomography, namely to learn the ground-state wave function of the transverse-field Ising chain (TFIC) based on measurements of the magnetization in a fixed spin basis $\{|x_1 \cdots x_M\rangle\}$, where $x_i = 0$ ($x_i = 1$) indicates that the i th spin points in the “up” (“down”) direction in the chosen basis. The Hamiltonian is $H = -\frac{1}{2} \sum_{i=1}^M (\sigma_i^x \sigma_{i+1}^x + g \sigma_i^z)$ with periodic boundary conditions and Pauli matrices σ_i^γ ($\gamma = x, y, z$) acting on site i . The model exhibits a quantum critical point at $|g| = 1$ and is integrable, such that the ground state $|\psi\rangle = \sum_x \psi(x) |x_1 \cdots x_M\rangle$ can be constructed explicitly [6, 62] (see also Supplementary Note 2A). As we consider measurements in the σ^z and σ^x directions only, the basis states $|x_1 \cdots x_M\rangle$ can be chosen such that $\psi(x)$ is real-valued and nonnegative, which allows us to employ the standard RBM architecture (1). (Generalizations for complex-valued wave functions are possible [7, 50].) The target distribution is thus

$$p(x) = \psi(x)^2.$$

Our second example (cf. Fig. 3) is closer in spirit to traditional machine-learning applications and involves pattern recognition and artificial image generation. The target distribution $p(x)$ generates 5×5 pixel images with a “hook” pattern comprised of 15 pixels (see Fig. 3a) implanted at a random position in a background of noisy pixels that are independently activated (white, $x_i = 1$) with probability $q = 0.1$ (see also Supplementary Note 2B for more details). Periodic boundary conditions are assumed, meaning that $p(x)$ is translationally invariant along the two image dimensions.

We also consider a one-dimensional variant of this example with only $M = 4$ ($M = 5$) visible units and an implanted “010” (“0110”) pattern, cf. Fig. 3d. In this case, we can solve the continuous-time learning dynamics ($\eta \rightarrow 0$ limit of (4)) for the exact target and model distributions $p(x)$ and $\hat{p}_\theta(x, h)$, obviating artifacts caused by insufficient training data or biased gradient approximations, see also Supplementary Note 1.

Our third example (cf. Fig. 4a–c) is a simplified digit reproduction task. Patterns of the ten digits 0 through 9 (see Fig. 4a) are selected and inserted uniformly at ran-

dom into image frames of 5×7 pixels, with the remaining pixels outside of the pattern again activated with probability $q = 0.1$ (see Supplementary Note 2C for details). No periodic boundary conditions are imposed, i.e., the input comprises proper, ordinary images.

In our fourth example (cf. Fig. 4d,e), we train RBMs on the MNIST dataset [8], which consists of 28×28 -pixel grayscale images of handwritten digits. It comprises a training set of 60 000 and a test set of 10 000 images. We convert the grayscale images with pixel values between 0 and 255 to binary data by mapping values $0 \dots 127$ to 0 and $128 \dots 255$ to 1 (see also Supplementary Note 2D).

ACKNOWLEDGMENTS

This work was supported by KAKENHI Grant No. JP22H01152 from the Japan Society for Promotion of Science.

The computer code for the numerical experiments can be accessed from the public repository <https://gitlab.com/lennartdw/xminirbm>.

[1] D. H. Ackley, G. E. Hinton, and T. J. Sejnowski, A learning algorithm for Boltzmann machines, *Cognitive Science* **9**, 147 (1985).

[2] P. Smolensky, Information processing in dynamical systems: foundations of harmony theory, in *Parallel Distributed Processing: Explorations in the Microstructure of Cognition*, Vol. 1, edited by D. E. Rumelhart and J. L. McClelland (MIT Press, 1986) pp. 194–281.

[3] G. E. Hinton and R. R. Salakhutdinov, Reducing the dimensionality of data with neural networks, *Science* **313**, 504 (2006).

[4] P. V. Gehler, A. D. Holub, and M. Welling, The rate adapting Poisson model for information retrieval and object recognition, in *Proceedings of the 23rd International Conference on Machine Learning*, ICML '06 (Association for Computing Machinery, New York, NY, USA, 2006) p. 337–344.

[5] G. E. Hinton, To recognize shapes, first learn to generate images, in *Computational Neuroscience: Theoretical Insights into Brain Function*, Progress in Brain Research, Vol. 165, edited by P. Cisek, T. Drew, and J. F. Kalaska (Elsevier, 2007) pp. 535–547.

[6] R. Salakhutdinov, A. Mnih, and G. Hinton, Restricted Boltzmann machines for collaborative filtering, in *Proceedings of the 24th International Conference on Machine Learning*, ICML '07 (Association for Computing Machinery, New York, NY, USA, 2007) p. 791–798.

[7] H. Larochelle and Y. Bengio, Classification using discriminative restricted Boltzmann machines, in *Proceedings of the 25th International Conference on Machine Learning*, ICML '08 (Association for Computing Machinery, New York, NY, USA, 2008) p. 536–543.

[8] G. Carleo, I. Cirac, K. Cranmer, L. Daudet, M. Schuld, N. Tishby, L. Vogt-Maranto, and L. Zdeborová, Machine learning and the physical sciences, *Rev. Mod. Phys.* **91**, 045002 (2019).

[9] P. Mehta, M. Bukov, C.-H. Wang, A. G. Day, C. Richardson, C. K. Fisher, and D. J. Schwab, A high-bias, low-variance introduction to machine learning for physicists, *Phys. Rep.* **810**, 1 (2019).

[7] G. Torlai, G. Mazzola, J. Carrasquilla, M. Troyer, R. Melko, and G. Carleo, Neural-network quantum state tomography, *Nat. Phys.* **14**, 447 (2018).

[11] G. Torlai and R. G. Melko, Latent space purification via neural density operators, *Phys. Rev. Lett.* **120**, 240503 (2018).

[12] G. Carleo and M. Troyer, Solving the quantum many-body problem with artificial neural networks, *Science* **355**, 602 (2017).

[13] Y. Nomura, A. S. Darmawan, Y. Yamaji, and M. Imada, Restricted Boltzmann machine learning for solving strongly correlated quantum systems, *Phys. Rev. B* **96**, 205152 (2017).

[14] X. Gao and L.-M. Duan, Efficient representation of quantum many-body states with deep neural networks, *Nat. Commun.* **8**, 662 (2017).

[15] I. Glasser, N. Pancotti, M. August, I. D. Rodriguez, and J. I. Cirac, Neural-network quantum states, string-bond states, and chiral topological states, *Phys. Rev. X* **8**, 011006 (2018).

[16] R. Xia and S. Kais, Quantum machine learning for electronic structure calculations, *Nat. Commun.* **9**, 4195 (2018).

[17] R. G. Melko, G. Carleo, J. Carrasquilla, and J. I. Cirac, Restricted Boltzmann machines in quantum physics, *Nat. Phys.* **15**, 887 (2019).

[18] K. Choo, A. Mezzacapo, and G. Carleo, Fermionic neural-network states for ab-initio electronic structure,

Nat. Commun. **11**, 2368 (2020).

[19] T. Kuremoto, S. Kimura, K. Kobayashi, and M. Obayashi, Time series forecasting using a deep belief network with restricted Boltzmann machines, Neurocomputing **137**, 47 (2014).

[20] M. Koch-Janusz and Z. Ringel, Mutual information, neural networks and the renormalization group, Nat. Phys. **14**, 578 (2018).

[21] P. M. Lenggenhager, D. E. Gökmen, Z. Ringel, S. D. Huber, and M. Koch-Janusz, Optimal renormalization group transformation from information theory, Phys. Rev. X **10**, 011037 (2020).

[2] G. E. Hinton, A practical guide to training restricted Boltzmann machines, in *Neural Networks: Tricks of the Trade: Second Edition*, edited by G. Montavon, G. B. Orr, and K.-R. Müller (Springer, Berlin, Heidelberg, 2012) pp. 599–619.

[4] A. Fischer and C. Igel, An introduction to restricted Boltzmann machines, in *Progress in Pattern Recognition, Image Analysis, Computer Vision, and Applications*, edited by L. Alvarez, M. Mejail, L. Gomez, and J. Jacobo (Springer, Berlin, Heidelberg, 2012) pp. 14–36.

[5] G. Montúfar, Restricted Boltzmann machines: Introduction and review (2018), arXiv:1806.07066.

[25] P. M. Long and R. A. Servedio, Restricted Boltzmann machines are hard to approximately evaluate or simulate, in *Proceedings of the 27th International Conference on International Conference on Machine Learning*, ICML’10 (Omnipress, Madison, WI, USA, 2010) p. 703–710.

[26] G. Desjardins, A. Courville, Y. Bengio, P. Vincent, and O. Delalleau, Tempered Markov chain Monte Carlo for training of restricted Boltzmann machines, in *Proceedings of the Thirteenth International Conference on Artificial Intelligence and Statistics*, Proceedings of Machine Learning Research, Vol. 9, edited by Y. W. Teh and M. Titterington (PMLR, Chia Laguna Resort, Sardinia, Italy, 2010) pp. 145–152.

[27] T. M. Cover and J. A. Thomas, *Elements of Information Theory*, 2nd ed. (Wiley, Hoboken, NJ, 2006).

[1] G. E. Hinton, Training products of experts by minimizing contrastive divergence, Neural Comput. **14**, 1771 (2002).

[3] T. Tieleman, Training restricted Boltzmann machines using approximations to the likelihood gradient, in *Proceedings of the 25th International Conference on Machine Learning*, ICML ’08 (Association for Computing Machinery, New York, NY, USA, 2008) p. 1064–1071.

[30] T. Tieleman and G. Hinton, Using fast weights to improve persistent contrastive divergence, in *Proceedings of the 26th Annual International Conference on Machine Learning*, ICML ’09 (Association for Computing Machinery, New York, NY, USA, 2009) p. 1033–1040.

[31] R. R. Salakhutdinov, Learning in Markov random fields using tempered transitions, in *Advances in Neural Information Processing Systems*, Vol. 22, edited by Y. Bengio, D. Schuurmans, J. Lafferty, C. Williams, and A. Culotta (Curran Associates, Inc., 2009).

[32] Y. Bengio and O. Delalleau, Justifying and generalizing contrastive divergence, Neural Comput. **21**, 1601–1621 (2009).

[33] A. Sokal, Monte Carlo methods in statistical mechanics: Foundations and new algorithms, in *Functional Integration: Basics and Applications*, edited by C. DeWitt-Morette, P. Cartier, and A. Folacci (Springer US, Boston, MA, 1997) pp. 131–192.

[34] A. Fischer and C. Igel, A bound for the convergence rate of parallel tempering for sampling restricted Boltzmann machines, Theoretical Computer Science **598**, 102 (2015).

[35] C. Tosh, Mixing rates for the alternating Gibbs sampler over restricted Boltzmann machines and friends, in *Proceedings of The 33rd International Conference on Machine Learning*, Proceedings of Machine Learning Research, Vol. 48, edited by M. F. Balcan and K. Q. Weinberger (PMLR, New York, NY, USA, 2016) pp. 840–849.

[36] S. Watanabe, Information theoretical analysis of multivariate correlation, IBM J. Res. Dev. **4**, 66 (1960).

[37] L. Younes, Synchronous boltzmann machines can be universal approximators, Appl. Math. Lett. **9**, 109 (1996).

[38] N. Le Roux and Y. Bengio, Representational Power of Restricted Boltzmann Machines and Deep Belief Networks, Neural Comput. **20**, 1631 (2008).

[39] G. Montúfar and J. Rauh, Hierarchical models as marginals of hierarchical models, Int. J. Approximate Reasoning **88**, 531 (2017).

[40] D. Sehayek, A. Golubeva, M. S. Albergo, B. Kulchytskyy, G. Torlai, and R. G. Melko, Learnability scaling of quantum states: Restricted Boltzmann machines, Phys. Rev. B **100**, 195125 (2019).

[8] Y. LeCun, C. Cortes, and C. J. C. Burges, The MNIST database of handwritten digits, <http://yann.lecun.com/exdb/mnist/>.

[42] M. A. Carreira-Perpiñán and G. E. Hinton, On contrastive divergence learning, in *10th International Workshop on Artificial Intelligence and Statistics (AISTATS)* (2005) p. 59.

[43] A. Fischer and C. Igel, Empirical analysis of the divergence of Gibbs sampling based learning algorithms for restricted Boltzmann machines, in *Artificial Neural Networks – ICANN 2010*, edited by K. Diamantaras, W. Duch, and L. S. Iliadis (Springer, Berlin, Heidelberg, 2010) pp. 208–217.

[44] H. Schulz, A. Müller, and S. Behnke, Investigating convergence of restricted Boltzmann learning, in *NIPS 2010 Workshop on Deep Learning and Unsupervised Feature Learning*, Vol. 1 (2010) p. 6.

[45] H. Manukian, Y. R. Pei, S. R. B. Bearden, and M. Di Ventra, Mode-assisted unsupervised learning of restricted Boltzmann machines, Commun. Phys. **3**, 105 (2020).

[46] K. Brügge, A. Fischer, and C. Igel, The flip-the-state transition operator for restricted Boltzmann machines, Machine Learning **93**, 53 (2013).

[47] C. Roussel, S. Cocco, and R. Monasson, Barriers and dynamical paths in alternating Gibbs sampling of restricted Boltzmann machines, Phys. Rev. E **104**, 034109 (2021).

[48] M. A. Petrovici, J. Bill, I. Bytschok, J. Schemmel, and K. Meier, Stochastic inference with spiking neurons in the high-conductance state, Phys. Rev. E **94**, 042312 (2016).

[49] A. F. Kungl, S. Schmitt, J. Klähn, P. Müller, A. Baumbach, D. Dold, A. Kugele, E. Müller, C. Koke, M. Kleider, C. Mauch, O. Breitwieser, L. Leng, N. Gürtler, M. Gürtler, D. Husmann, K. Husmann, A. Hartel, V. Karasenko, A. Grübl, J. Schemmel, K. Meier, and M. A. Petrovici, Accelerated physical emulation of bayesian inference in spiking neural networks, Front. Neurosci. **13**, 1201 (2019).

[50] S. Czischek, J. M. Pawłowski, T. Gasenzer, and M. Gärttner, Sampling scheme for neuromorphic simulation of entangled quantum systems, Phys. Rev. B **100**, 195120 (2019).

- [51] S. Czischek, A. Baumbach, S. Billaudelle, B. Cramer, L. Kades, J. M. Pawłowski, M. K. Oberthaler, J. Schemmel, M. A. Petrovici, T. Gasenzer, and M. Gärttner, Spiking neuromorphic chip learns entangled quantum states, *SciPost Phys.* **12**, 39 (2022).
- [52] R. Klassert, A. Baumbach, M. A. Petrovici, and M. Gärttner, Variational learning of quantum ground states on spiking neuromorphic hardware (2021), arXiv:2109.15169.
- [53] H. Manukian, F. L. Traversa, and M. Di Ventra, Accelerating deep learning with memcomputing, *Neural Networks* **110**, 1 (2019).
- [54] S. H. Adachi and M. P. Henderson, Application of quantum annealing to training of deep neural networks (2015), arXiv:1510.06356.
- [55] M. Benedetti, J. Realpe-Gómez, R. Biswas, and A. Perdomo-Ortiz, Estimation of effective temperatures in quantum annealers for sampling applications: A case study with possible applications in deep learning, *Phys. Rev. A* **94**, 022308 (2016).
- [56] J. Martens, A. Chattopadhyay, T. Pitassi, and R. Zemel, On the representational efficiency of restricted Boltzmann machines, in *Advances in Neural Information Processing Systems*, Vol. 26, edited by C. J. C. Burges, L. Bottou, M. Welling, Z. Ghahramani, and K. Q. Weinberger (Curran Associates, Inc., 2013).
- [57] S.-I. Amari, Information geometry on hierarchy of probability distributions, *IEEE Trans. Inf. Theory* **47**, 1701 (2001).
- [58] N. Le Roux, N. Heess, J. Shotton, and J. Winn, Learning a Generative Model of Images by Factoring Appearance and Shape, *Neural Comput.* **23**, 593 (2011), https://direct.mit.edu/neco/article-pdf/23/3/593/849559/neco_a_00086.pdf.
- [59] H. W. Lin, M. Tegmark, and D. Rolnick, Why does deep and cheap learning work so well?, *J. Stat. Phys.* **168**, 1223 (2017).
- [60] A. M. Saxe, J. L. McClelland, and S. Ganguli, A mathematical theory of semantic development in deep neural networks, *Proceedings of the National Academy of Sciences* **116**, 11537 (2019).
- [61] E. Romero Merino, F. Mazzanti Castrillejo, and J. Delgado Pin, Neighborhood-based stopping criterion for contrastive divergence, *IEEE Trans. Neural Netw. Learn. Syst.* **29**, 2695 (2018).
- [62] P. Pfeuty, The one-dimensional Ising model with a transverse field, *Ann. Phys.* **57**, 79 (1970).
- [6] L. Vidmar and M. Rigol, Generalized Gibbs ensemble in integrable lattice models, *J. Stat. Mech: Theory Exp.* **2016**, 064007 (2016).

SUPPLEMENTARY INFORMATION

Labels of equations, figures, tables, and references in these Supplementary Notes are prefixed by a capital letter “S” (e.g., Fig. S1, Eq. (S3)). Any plain labels (e.g., Fig. 1, Eq. (3)) refer to the corresponding items in the main text.

S1. TRAINING DETAILS

With the exception of Fig. 3e, the data presented in the main text were obtained from RBMs trained with a stochastic gradient descent scheme based on the ideal gradient descent updates from Eq. (4) of the main text and utilizing contrastive divergence (CD, see Refs. [S1, S2]) or persistent contrastive divergence (PCD, see Ref. [S3]) to approximate the model averages. Concretely, the training dataset $S = \{\tilde{x}^{(1)}, \dots, \tilde{x}^{|S|}\}$ was partitioned randomly into $s := \frac{|S|}{B}$ minibatches S_1, \dots, S_s of size B at the beginning of each epoch t . We recall that Markov chains of the form

$$x^{(0)} \rightarrow h^{(0)} \rightarrow x^{(1)} \rightarrow h^{(1)} \rightarrow \dots \quad (S1)$$

are employed to assess the model distribution approximately (cf. Eq. (5) of the main text). We denote a particular (random) realization of $x^{(n)}$ and $h^{(n)}$ for a chain initiated at a (fixed) $x^{(0)} = \tilde{x}$ by $\hat{x}^{(n)}(\tilde{x})$ and $\hat{h}^{(n)}(\tilde{x})$, respectively. In CD, the updates (4) are then approximated as

$$\begin{aligned} w_{ij}(t + \frac{r}{s}) - w_{ij}(t + \frac{r-1}{s}) \\ = \frac{\eta}{B} \sum_{\tilde{x} \in S_r} \left[\tilde{x}_i \hat{h}_j^{(0)}(\tilde{x}) - \hat{x}_i^{(n_{CD})}(\tilde{x}) \hat{h}_j^{(n_{CD})}(\tilde{x}) \right], \end{aligned} \quad (S2a)$$

$$\begin{aligned} a_i(t + \frac{r}{s}) - a_i(t + \frac{r-1}{s}) \\ = \frac{\eta}{B} \sum_{\tilde{x} \in S_r} \left[\tilde{x}_i - \hat{x}_i^{(n_{CD})}(\tilde{x}) \right], \end{aligned} \quad (S2b)$$

$$\begin{aligned} b_j(t + \frac{r}{s}) - b_j(t + \frac{r-1}{s}) \\ = \frac{\eta}{B} \sum_{\tilde{x} \in S_r} \left[\hat{h}_j^{(0)}(\tilde{x}) - \hat{h}_j^{(n_{CD})}(\tilde{x}) \right] \end{aligned} \quad (S2c)$$

for $r = 1, \dots, s$. In essence, the model averages in (4) are thus approximated by empirical averages over samples from Markov chains (S1) that are initialized with a training sample $x^{(0)} = \tilde{x} \in S$. If Δ_θ is sufficiently small, such $x^{(0)}$ from S may already be a reasonable approximation for a sample from $\hat{p}_\theta(x)$, and the chain generates a new (but correlated) sample. In the beginning of training, when $\hat{p}_\theta(x)$ is still far from $p(x)$, such an initialization of the chains is less justified, but it is found to work in practice [S2, S4, S5], not least because the mixing and

autocorrelation times of the chains are typically small as well in this case.

In PCD, the updates (4) are approximated as

$$\begin{aligned} w_{ij}(t + \frac{r}{s}) - w_{ij}(t + \frac{r-1}{s}) \\ = \eta \left[\frac{1}{B} \sum_{\tilde{x} \in S_r} \tilde{x}_i \hat{h}_j^{(0)}(\tilde{x}) - \frac{1}{L} \sum_{x' \in Q(t + \frac{r}{s})} x'_i \hat{h}_j^{(0)}(x') \right], \end{aligned} \quad (S3a)$$

$$\begin{aligned} a_i(t + \frac{r}{s}) - a_i(t + \frac{r-1}{s}) \\ = \eta \left[\frac{1}{B} \sum_{\tilde{x} \in S_r} \tilde{x}_i - \frac{1}{L} \sum_{x' \in Q(t + \frac{r}{s})} x'_i \right], \end{aligned} \quad (S3b)$$

$$\begin{aligned} b_j(t + \frac{r}{s}) - b_j(t + \frac{r-1}{s}) \\ = \eta \left[\frac{1}{B} \sum_{\tilde{x} \in S_r} \hat{h}_j^{(0)}(\tilde{x}) - \frac{1}{L} \sum_{x' \in Q(t + \frac{r}{s})} \hat{h}_j^{(0)}(x') \right], \end{aligned} \quad (S3c)$$

$$Q(t + \frac{r}{s}) = \left\{ \hat{x}^{(n_{CD})}(x') : x' \in Q(t + \frac{r-1}{s}) \right\} \quad (S3d)$$

for $r = 1, \dots, s$, where $Q(0)$ is a set of random, independent configurations of the visible units and $L := |Q(0)|$. We always use $L = B$. Hence the model averages are approximated by empirical averages over samples from Markov chains (S1) that are initialized with (or, in other words, continued from) samples of the previous update step, i.e., the chains are *persistent*. Note, however, that the model distribution used to generate (or advance) the chains changes from step to step as the model parameters θ change. If these parameter updates are sufficiently small and the initial configurations $x' \in Q(0)$ emulate samples from the initial model $\hat{p}_{\theta(0)}(x)$, the chains approximately reflect the gradually evolving stationary model distribution throughout the training process. However, subsequent samples are generally not independent, especially if $n_{CD} \lesssim \tau_\theta$.

The total number of training epochs in Figs. 2–4 of the main paper as well as in this Supplementary Information varies between 2×10^4 and 3×10^6 , depending on the time needed until improvement of the accuracy could no longer be observed and extending reasonably far beyond it to capture the degradation regime. As mentioned in the main text, the machines were initialized by drawing the parameters $\theta_k(0)$ independently from a normal distribution $\mathcal{N}(\mu, \sigma)$ of mean μ and standard deviation σ , namely $w_{ij}(0) \sim \mathcal{N}(0, 10^{-2})$ and $a_i(0), b_j(0) \sim \mathcal{N}(0, 10^{-1})$ (Figs. 2, 3, and 4b,c) or $a_i = b_j = 0$ (Fig. 4e). Figs. 2 and 3 show averages over 5 independent repetitions of the experiment for each hyperparameter configuration. Fig. 4 shows results for single machines.

For the data in Fig. 3e, we utilized—as described in the main text—the full target distribution $p(x)$ and the exact

n -step CD model distribution $\hat{p}_\theta^{(n)}$ or the full model distribution $\hat{p}_\theta(x)$ for the expectation values. Moreover, we employed the continuous-time limit of the update equations (4). Hence the evolution of the weights is governed by the differential equations

$$\dot{w}_{ij}(t) = \sum_{x,h} x_i h_j \hat{p}_{\theta(t)}(h|x) \left[p(x) - \hat{p}_{\theta(t)}^{(n)}(x) \right], \quad (\text{S4a})$$

$$\dot{a}_i(t) = \sum_x x_i \left[p(x) - \hat{p}_{\theta(t)}^{(n)}(x) \right], \quad (\text{S4b})$$

$$\dot{b}_j(t) = \sum_{x,h} h_j \hat{p}_{\theta(t)}(h|x) \left[p(x) - \hat{p}_{\theta(t)}^{(n)}(x) \right], \quad (\text{S4c})$$

where the dots indicate derivatives with respect to t and

$$\hat{p}_\theta^{(n)}(x) := \sum_{x',h'} \hat{p}_\theta(x|h') \hat{p}_\theta(h'|x') \hat{p}_\theta^{(n-1)}(x'), \quad (\text{S5})$$

$$\hat{p}_\theta^{(0)}(x) := p(x), \quad (\text{S6})$$

and $\hat{p}_\theta^{(\infty)}(x) \equiv \hat{p}_\theta(x)$. We then integrated Eqs. (S4) numerically (starting from random initial conditions as before) using *Mathematica*'s `NDSolve` routine.

S2. EXAMPLE TASKS

A. Transverse-field Ising chain

The transverse-field Ising chain (TFIC) with M sites is defined by the Hamiltonian

$$H = -\frac{1}{2} \sum_{i=0}^{M-1} (\sigma_i^x \sigma_{i+1}^x + g \sigma_i^z) \quad (\text{S7})$$

with periodic boundary conditions, $\sigma_{i+M}^\gamma = \sigma_i^\gamma$, where σ_i^γ ($\gamma = x, y, z$) are the Pauli matrices acting on site i . The corresponding spin raising and lowering operators are $\sigma_i^\pm := \frac{1}{2}(\sigma_i^x \pm i\sigma_i^y)$.

The Hamiltonian can be diagonalized by the following sequence of transformations: the Jordan-Wigner transformation

$$c_i := P_i \sigma_i^- \quad (\text{S8})$$

with $P_i := \prod_{j=0}^{i-1} (-\sigma_j^z)$, the Fourier transformation

$$\tilde{c}_k := \frac{1}{\sqrt{L}} \sum_i e^{-ik_i} c_i \quad (\text{S9})$$

with fermionic (bosonic) Matsubara frequencies k if the total particle number $\sum_i c_i^\dagger c_i$ is even (odd), and the Bogoliubov transformation

$$\eta_k := u_k \tilde{c}_k - v_k \tilde{c}_{-k}^\dagger \quad (\text{S10})$$

TABLE S1. Entropy $S(p)$ and total correlation $C_{\text{tot}}(p)$ of the TFIC ground-state distribution in the σ^z and σ^x bases for various values of the magnetic-field strength g .

g	σ^z basis		σ^x basis	
	$S(p)$	$C_{\text{tot}}(p)$	$S(p)$	$C_{\text{tot}}(p)$
0.5	12.48	0.705	1.216	12.65
0.8	10.99	0.824	5.062	8.801
1	8.028	1.441	8.721	5.142
1.2	4.808	1.891	11.38	2.478
2	1.760	1.134	13.17	0.689
4	0.523	0.400	13.70	0.160

with $u_k := (\varepsilon_k + \alpha_k)/\omega_k$, $v_k := i\beta_k/\omega_k$, $\alpha_k := -2J(g + \cos k)$, $\beta_k := 2J \sin k$, $\varepsilon_k^2 := \alpha_k^2 + \beta_k^2$, $\omega_k^2 := 2\varepsilon_k(\varepsilon_k + \alpha_k)$; see, for example, Ref. [S6]. The resulting Hamiltonian is

$$H = \sum_k \varepsilon_k \left(\eta_k^\dagger \eta_k - \frac{1}{2} \right) \quad (\text{S11})$$

in the sector with an even number of particles, to which the ground state belongs. This ground state can be constructed as

$$|\psi\rangle := \prod_k \frac{1}{|v_k|} \eta_k \eta_{-k} |\downarrow \cdots \downarrow\rangle \quad (\text{S12})$$

from the state $|\downarrow \cdots \downarrow\rangle$ with all spins down in the σ^z basis [S6].

Moreover, by adjusting the global phase, it can be written such that $\psi(x) := \langle x_0 \cdots x_{M-1} | \psi \rangle$ is real-valued and nonnegative when $|x_0 \cdots x_{M-1}\rangle$ is a basis state in the σ^z or σ^x bases. For our quantum-state tomography task of the ground-state wave function from measurements in either of the two bases, we can therefore take the target distribution as $p(x) := \psi(x)^2$ and do not need additional modifications of the RBM model to facilitate the phase reconstruction [S7].

Tab. S1 lists the entropy $S(p) := -\sum_x p(x) \ln p(x)$ and total correlation $C_{\text{tot}}(p)$ (cf. Eq. (8) of the main text) of the target distribution obtained for various values of g .

B. Hook-pattern images

We consider $L \times L$ images $x = (x_{i_1, i_2})_{i_1, i_2=0}^{L-1}$ whose pixels $x_i = x_{i_1, i_2}$ are either black ($x_i = 0$) or white ($x_i = 1$). We denote the set of all $2^{L \times L}$ of these images by \mathcal{K} .

The characteristic feature of the target distribution $p(x)$ is a “hook” pattern comprised of a total of 15 pixels, cf. Fig. 3a. We assume periodic boundary conditions ($x_{i,j} = x_{i+L,j} = x_{i,j+L}$) and denote the max-distance on the image grid by

$$d_\infty(i, j) = \max_{\mu=1,2} \min\{|i_\mu - j_\mu|, L - |i_\mu - j_\mu|\}. \quad (\text{S13})$$

Similarly, for a set of pixel positions (sites) I and a single site j , define $d_\infty(I, j) := \min\{d_\infty(i, j) : i \in I\}$. An image

x then shows the “hook” pattern at site i if the pixels at sites $I_0(i) := \{(i_1, i_2), (i_1 - 1, i_2), (i_1, i_2 + 1)\}$ are white and the pixels at sites $I_1(i) := \{j : d_\infty(I_0(i), j) = 1\}$ are black. In other words, $x_j = 1$ for all $j \in I_0(i)$ and $x_j = 0$ for all $j \in I_1(i)$. The remaining $L^2 - 15$ pixels at sites $I_{\geq 2}(i) := \{j : d_\infty(I_0(i), j) \geq 2\}$ can take arbitrary values. We denote the set of all images with a “hook” pattern at an arbitrary site by \mathcal{K}_H . In the main text, we choose $L = 5$; examples are shown in Fig. 3a. Note that there are a total of $|\mathcal{K}_H| = L^2 \times 2^{L^2-15} = 25\,600$ images exhibiting the pattern, which is a fraction of $|\mathcal{K}_H|/|\mathcal{K}| = 25 \times 2^{-15} \approx 0.08\%$ of all 5×5 images.

The target distribution picks a random location $i = (i_1, i_2)$ for the hook pattern and activates all remaining pixels in $I_{\geq 2}(i)$ with probability $q = \frac{1}{10}$. Hence

$$p(x) = \mathbb{1}_{\mathcal{K}_H}(x) \sum_i \prod_{j \in I_{\geq 2}(i)} [x_j q + (1 - x_j)(1 - q)], \quad (\text{S14})$$

where $\mathbb{1}_S$ is the indicator function of the set S , i.e., $\mathbb{1}_S(x) = 1$ if $x \in S$ and 0 otherwise.

The entropy is $S(p) \approx 6.47$ and the total correlation is $C_{\text{tot}}(p) \approx 4.53$.

The one-dimensional, smaller distributions from Fig. 3d are structurally similar, but involve a core pattern of white pixels at sites $I_0(i)$ of only one ($M = 4$) or two ($M = 5$) pixels, surrounded by one-site boundaries $I_1(i)$ of black pixels in either direction, with the remaining pixel in $I_{\geq 2}(i)$ being arbitrary again.

C. Digit images

We consider $H \times W$ images $x = (x_{i_1, i_2})$ with pixel values $x_i = x_{i_1, i_2} \in \{0, 1\}$ and denote the set of all such images by \mathcal{K} .

The target distribution involves images showing one of ten patterns representing the digits 0 through 9 (cf. Fig. 4a of the main text). The digit patterns consist of a core block of fixed black or white pixels (black or white in Fig. 4a) as well as a boundary (gray-shaded in Fig. 4a) which may either be represented by black pixels or by the image frame (i.e., the gray pixels may lie “out of bounds”). No periodic boundary conditions are assumed. The remaining pixels outside of the respective pattern may take arbitrary values. Due to the different sizes of the digit patterns, the number of possible images for each pattern is different in general. We denote the set of all images with a “ k ” pattern by \mathcal{K}_k . For $H = 7$ and $W = 5$, which is our choice for the data shown in Fig. 4a–c of the main text, the resulting cardinalities of the sets \mathcal{K}_k are summarized in Tab. S2.

The target distribution selects a pattern k uniformly at random, $p(x \in \mathcal{K}_k) = \frac{1}{10} \mathbb{1}_{\bigcup_i \mathcal{K}_i}(x)$. The selected pattern is then placed at a random position $i = (i_1, i_2)$ with uniform probability $p(x \in \mathcal{K}_{k,i} | x \in \mathcal{K}_k)$, where $\mathcal{K}_{k,i}$ is the set of all images showing pattern k at position i .

TABLE S2. Cardinalities of the sets \mathcal{K}_k of digit images. In total, $|\mathcal{K}_{\text{PN}}| = 40\,507\,353$ out of the total of $2^{7 \times 5} = 34\,359\,738\,368$ possible images show digit patterns.

k	$ \mathcal{K}_k $	k	$ \mathcal{K}_k $
0	8\,513	5	565\,391
1	38\,558\,138	6	56\,464
2	565\,391	7	66\,624
3	565\,391	8	8\,513
4	56\,464	9	56\,464

Due to the different pattern shapes, again, the admissible positions are generally different for different patterns. Denoting the set of all pixel sites that are not part of the pattern k at position i by $\bar{I}(k, i)$, the remaining pixels represent noise and are white independently with probability $q = \frac{1}{10}$, i.e., $p(x_j = 1 | j \in \bar{I}(i, k)) = q$. The total probability of a given image x is thus

$$p(x) = \sum_k p(x \in \mathcal{K}_k) \sum_i p(x \in \mathcal{K}_{k,i} | x \in \mathcal{K}_k) \times \prod_{j \in \bar{I}(k, i)} [x_j q + (1 - x_j)(1 - q)]. \quad (\text{S15})$$

Note that an image can “accidentally” have patterns at multiple positions; for the image sizes we adopted, in particular, this can happen if one of them is the “1” pattern.

The entropy of this distribution is $S(p) \approx 8.35$ and the total correlation is $C_{\text{tot}}(p) \approx 11.67$.

For the empirical loss measure $\tilde{\Delta}_\sigma^{(T, \hat{T})}$ in Fig. 4c, the parameter σ is determined by minimizing $\tilde{\Delta}_\sigma^{(T, S)}$ between the test and training datasets of $|T| = 10\,000$ and $|S| = 50\,000$ samples, respectively. From the relationship shown in Fig. S1a, we find $\tilde{\Delta}_\sigma^{(T, S)} \approx 1.354$ at $\sigma \approx 0.32$ for the minimum.

D. MNIST

We use the MNIST dataset of 28×28 -pixel images of handwritten digits with its standard splitting into $|S| = 60\,000$ training and $|T| = 10\,000$ test images [S8]. Each subset contains equal fractions of representations for each digit. The grayscale pixel values $z_i \in \{0, 1, \dots, 255\}$ are preprocessed as $x_i = \lfloor \frac{z_i}{128} \rfloor$ to obtain a binary dataset. The entropies of the thus-obtained training and test datasets are $S(\tilde{p}(\cdot; S)) \approx 11.00$ and $S(\tilde{p}(\cdot; T)) \approx 9.21$, and their total correlations are $C_{\text{tot}}(\tilde{p}(\cdot; S)) \approx 195.0$ and $C_{\text{tot}}(\tilde{p}(\cdot; T)) \approx 196.5$, respectively.

Similarly as before, the parameter σ for $\tilde{\Delta}_\sigma^{(T, \hat{T})}$ in Fig. 4e is chosen such that $\tilde{\Delta}_\sigma^{(T, S)}$ becomes minimal. As shown in Fig. S1b, we obtain $\tilde{\Delta}_\sigma^{(T, S)} \approx 147.4$ at $\sigma \approx 0.41$ for that minimum.

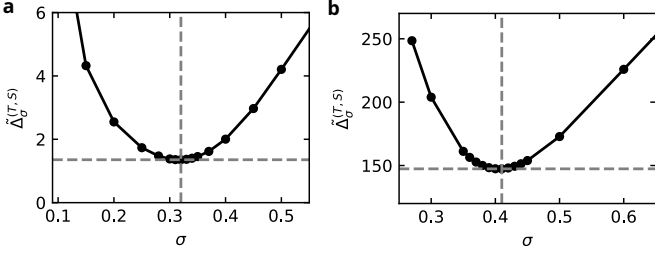


FIG. S1. Kullback-Leibler divergence $\tilde{\Delta}_\sigma^{(T,S)} := D_{\text{KL}}(\tilde{p}(\cdot; T) \parallel \tilde{p}_\sigma(\cdot; S))$ between the empirical distribution of the test data $\tilde{p}(x; T)$ and the Gaussian-smoothened empirical distribution $\tilde{p}_\sigma(x; S)$ of the training data as a function of the smoothening width parameter σ . The value of σ for which $\tilde{\Delta}_\sigma^{(T,S)}$ becomes minimal is adopted in Fig. 4 to calculate the empirical loss measure $\tilde{\Delta}_\sigma^{(T,\hat{T})}$.

S3. INITIALIZATION SCHEMES

As argued in the main text, the most natural way to initialize the RBM parameters $(\theta_k) = (w_{ij}, a_i, b_j)$ is to assign small random values to them if no information about the target distribution $p(x)$ is available. In the main text, we thus sample the initial θ_k from independent normal distributions $\mathcal{N}(\mu, \sigma)$ with vanishing mean $\mu = 0$ and small (or vanishing) standard deviation σ . In Figs. S2 and S3, we compare the resulting relationship between Δ_θ and τ_θ for other initialization schemes.

One piece of information about the target distribution that is easily accessible is the approximate value of the marginal probabilities $p_i(x_i)$ of the visible units. Hence Hinton [S2] suggests to initialize the visible-unit biases as $a_i = \ln[\nu_i / (1 - \nu_i)]$, where $\nu_i := \frac{1}{|S|} \sum_{\tilde{x} \in S} \tilde{x}_i$ is the frequency of $x_i = 1$ in the training dataset S , i.e., $p_i(x_i = 1) \approx \nu_i$. In the numerical examples from the second columns of Figs. S2 and S3, we cap the so-obtained a_i at 2 in absolute value. For the weights and hidden-unit biases, Ref. [S2] suggests using $w_{ij} \sim \mathcal{N}(0, 0.01)$ and $b_j = 0$. Following this scheme, one can shorten the independent-learning period as can be seen in the second columns of Figs. S2 and S3. Nevertheless, we observe the same learning characteristics as for the fully random initialization in the correlation-learning and degradation regimes.

By accident or deliberation, the initial model distribution may already exhibit noticeable but spurious correlations as well. This is exemplified in the last three columns of Figs. S2 and S3. Such initial correlations may arise, for instance, if the weights are chosen too large (third columns) or if parameters from a pre-trained machine using a different target distribution are adopted (fourth and fifth columns). In the case of such spurious initial correlations, the machine typically starts further away from the lower bound (7). As training progresses, however, the bound is approached by decreasing both Δ_θ and τ_θ first and eventually showing similar tradeoff characteristics as in the “independent” initialization schemes (first

two columns).

S4. AUTOCORRELATION TIMES OF DIFFERENT OBSERVABLES

As explained in the main text (see Methods), different observables $f(x)$ generally exhibit different integrated autocorrelation times $\tau_\theta^{(f)}$. We recall that the latter are defined as

$$\tau_\theta^{(f)} := 1 + 2 \sum_{n=1}^{\infty} \frac{g_\theta^{(f)}(n)}{g_\theta^{(f)}(0)}, \quad (\text{S16})$$

where

$$g_\theta^{(f)}(n) := \langle f(x^{(0)}) f(x^{(n)}) \rangle - \langle f(x^{(0)}) \rangle^2 \quad (\text{S17})$$

is the correlation function of $f(x)$ for the Markov chain (S1) initialized in the stationary state $x^{(0)} \sim \hat{p}_\theta(x)$ (cf. Eqs. (15) and (16) in the main text).

The quantity τ_θ from Eq. (6), which is our principal measure of sampling efficiency in the main text, is a weighted average of the autocorrelation times $\tau_\theta^{(x_i)}$ of the individual visible units $f(x) = x_i$ (see Eq. (18)). In the following, we verify that the autocorrelation times $\tau_\theta^{(f)}$ typically scale similarly to τ_θ . More precisely, they are found to be largely proportional to each other. For the power-law bound (7) which quantifies the accuracy–efficiency tradeoff, this changes the constant c on the right-hand side to an observable-dependent $c^{(f)}$. Those constants can no longer be identified with the total correlation $C_{\text{tot}}(p)$ of the full target distribution $p(x)$. Instead, the pertinent reference should be a characteristic of the distribution $p(f(x))$ of the transformed variables, for which, however, it may not always be possible or reasonable to define a “total correlation.”

In Fig. S4, we adopt the same setup and RBMs as in the third column of Fig. 2b of the main text (TFIC, σ^z basis, $n_{\text{CD}} = 1$, $|S| = 25\,000$). We plot the integrated autocorrelation times $\tau_\theta^{(f)}$ for various observables against τ_θ . Concretely, the investigated observables are

- the individual visible units,

$$f(x) = x_i; \quad (\text{S18a})$$

- the nearest-neighbor correlation function,

$$f(x) = x_i x_{i+1}; \quad (\text{S18b})$$

- the next-nearest neighbor correlation function,

$$f(x) = x_i x_{i+2}; \quad (\text{S18c})$$

- the 3-point nearest-neighbor correlation function,

$$f(x) = x_i x_{i+1} x_{i+2}. \quad (\text{S18d})$$

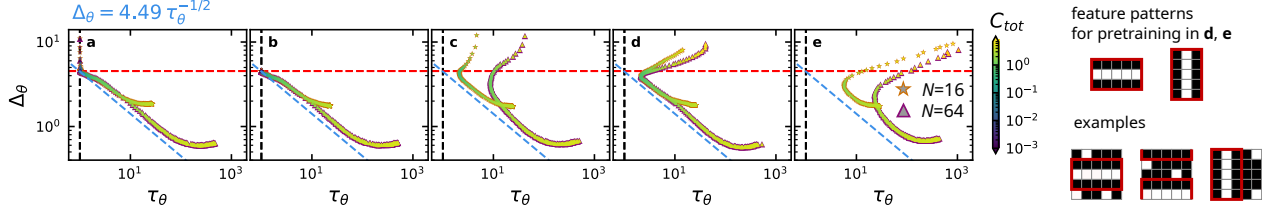


FIG. S2. Exact loss Δ_θ vs. autocorrelation time τ_θ for various initialization schemes of the weights in the pattern recognition task from Fig. 3 (see also Sec. S2B). Initialization schemes: (a) $w_{ij} \sim \mathcal{N}(0, 0.01)$, $a_i, b_j \sim \mathcal{N}(0, 0.1)$ (similar to the main text); (b) $w_{ij} \sim \mathcal{N}(0, 0.01)$, $a_i = \ln[\nu_i / (1 - \nu_i)]$ with $\nu_i := \frac{1}{|S|} \sum_{\tilde{x} \in S} \tilde{x}_i$ the activation frequency of the i th visible unit in the training dataset S , $b_j = 0$ [S2]; (c) $w_{ij}, a_i, b_j \sim \mathcal{N}(0, 1)$; (d) snapshot after $t = 500$ training epochs of a machine initialized like in (a) and subsequently trained on images with horizontal or vertical line patterns (see sketch) and otherwise identical hyperparameters; (e) similar to (d), but using snapshots after $t = 50\,000$ training epochs. Data points show averages over 5 independent runs for each scheme. Fill colors indicate the total correlation $C_{\text{tot}}(\hat{p}_\theta)$ of the model distribution (see colorbar), border colors and marker types indicate the number of hidden units N (see legend in (e)). Further hyperparameters: CD training with $n_{\text{CD}} = 1$, $\eta = 0.005$, $B = 100$, $|S| = 5000$.

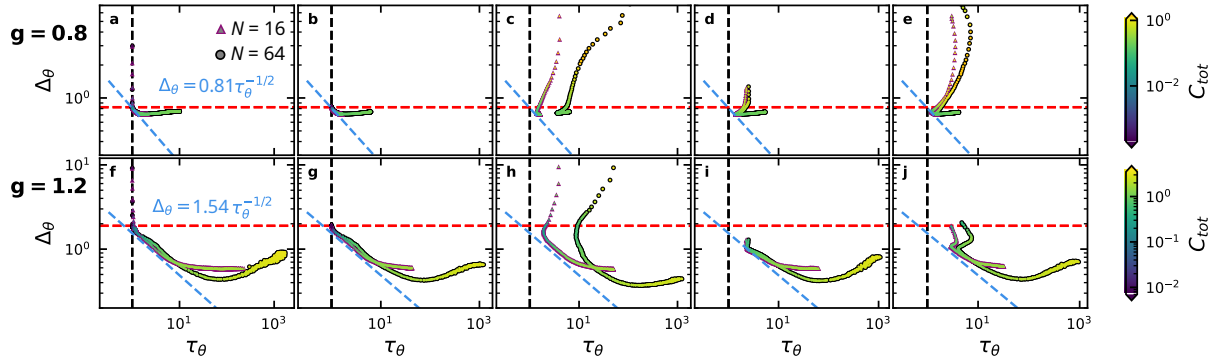


FIG. S3. Exact loss Δ_θ vs. autocorrelation time τ_θ for various initialization schemes of the weights in the ground-state tomography task for the TFIC with $g = 0.8$ (top row) and $g = 1.2$ (bottom row), cf. Fig. 2 and Sec. S2A). Initialization schemes: (a,f) $w_{ij} \sim \mathcal{N}(0, 0.01)$, $a_i, b_j \sim \mathcal{N}(0, 0.1)$ (similar to the main text); (b,g) $w_{ij} \sim \mathcal{N}(0, 0.01)$, $a_i = \ln[\nu_i / (1 - \nu_i)]$ with $\nu_i := \frac{1}{|S|} \sum_{\tilde{x} \in S} \tilde{x}_i$ the activation frequency of the i th visible unit in the training dataset S , $b_j = 0$ [S2]; (c,h) $w_{ij}, a_i, b_j \sim \mathcal{N}(0, 1)$; (d,i) snapshot after $t = 5000$ training epochs of a machine initialized like in (a,f) and subsequently trained to learn the ground state for $g = 1$ and otherwise identical hyperparameters; (e,j) similar to (d,i), but using snapshots after $t = 5000$ training epochs when learning the $g = 2$ ground state. Data points show averages over 5 independent runs for each scheme. Fill colors indicate the total correlation $C_{\text{tot}}(\hat{p}_\theta)$ of the model distribution (see colorbars), border colors and marker types indicate the number of hidden units N (see legend in (a)). Further hyperparameters: CD training with $n_{\text{CD}} = 1$, $\eta = 0.001$, $B = 100$, $|S| = 25\,000$.

Note that, due to translational invariance of the target distribution $p(x)$, all those observables should be independent of the reference index $i \in \{1, \dots, M\}$. However, the learned model distribution $\hat{p}_\theta(x)$ may not fully reflect this symmetry. The autocorrelation time $\tau_\theta^{(f)}$ shown in Fig. S4 is therefore averaged over all indices i . We also show the autocorrelation time for the general 2-point correlation function

$$f(x) = x_{i_1} x_{i_2}, \quad i_1, i_2 \in \{1, \dots, M\}, \quad (\text{S19})$$

again averaged over all pairs (i_1, i_2) . (Note that this observable still depends on the difference $i_1 - i_2$ though.) Finally, we also include autocorrelation times for the mean over all visible units,

$$f(x) = \frac{1}{M} \sum_i x_i. \quad (\text{S20})$$

We point out that there are RBM configurations for which we did not obtain a reliable estimate of τ_θ or $\tau_\theta^{(f)}$ within the maximally admitted number of sampling steps (see also Methods in the main text). Therefore, the data points are sparser for $N = 64$, in particular.

As mentioned above, the results indicate that $\tau_\theta^{(f)}$ is usually proportional to $f(x)$. With regard to the seemingly largest (relative) deviations in the top-left panel, we observe that the autocorrelation times are generally very small in this case. We also remark that, due to translation invariance, the trained models should satisfy $\tau_\theta^{(x_i)} = \tau_\theta$ if they realized this symmetry exactly. Deviations from this ideal behavior can hint at overfitting and insufficient expressivity.

The same conclusions can be drawn from Fig. S5, which shows autocorrelation times for different observ-

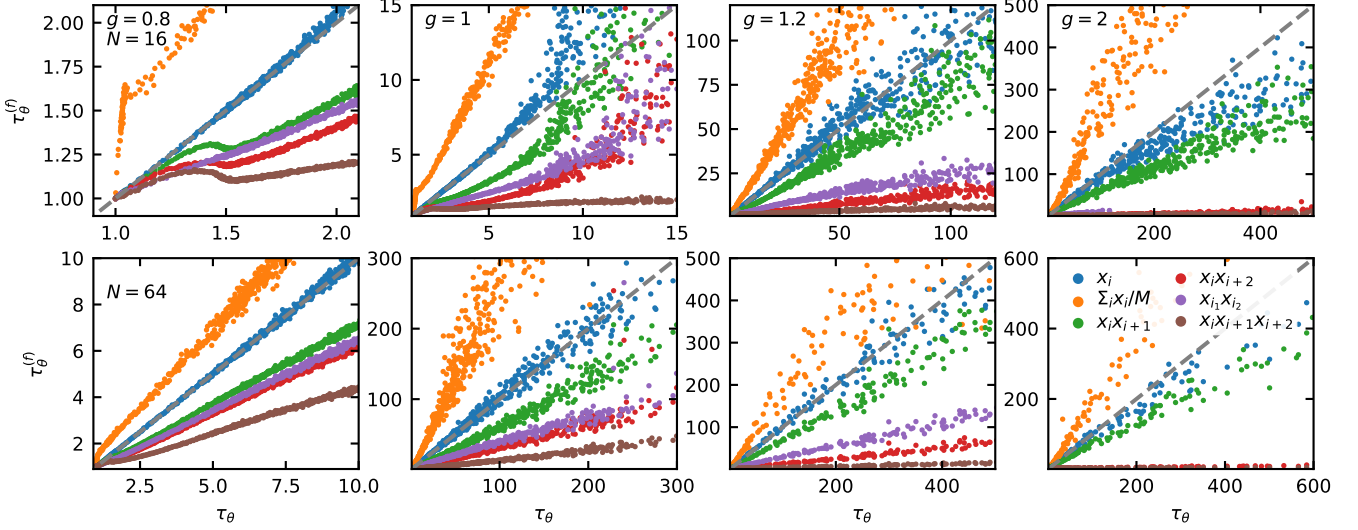


FIG. S4. Integrated autocorrelation times $\tau_\theta^{(f)}$ (cf. Eqs. (S18)–(S20)) for various observables $f(x)$ (see legend in the bottom-right panel) vs. sampling efficiency τ_θ in the transverse-field Ising chain (TFIC, cf. Fig. 2 and Sec. S2 A) in the σ^z basis. The panels show results for different external fields g (cf. Eq. (S7)) in the columns and different numbers of hidden units N in the rows as indicated. Hyperparameters: $n_{CD} = 1$, $\eta = 10^{-3}$, $B = 100$, $|S| = 25\,000$. For observables depending on the visible-unit indices i, i_1, i_2 , the data are averaged over all those indices. Furthermore, as in the main text, each data point is an average over five independently trained RBMs at a fixed training epoch t . The gray dashed line shows the function $\tau_\theta^{(f)} = \tau_\theta$ for reference.

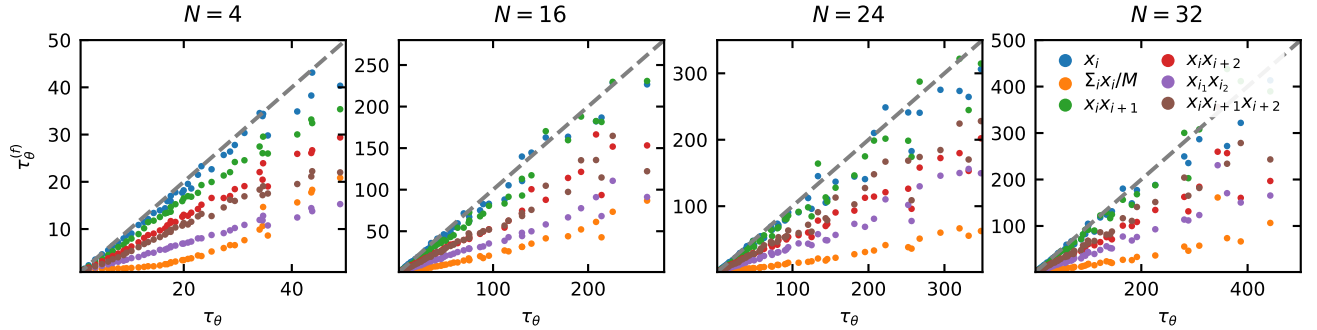


FIG. S5. Integrated autocorrelation times $\tau_\theta^{(f)}$ (cf. Eqs. (S18)–(S20)) for various observables $f(x)$ (see legend in the right-most panel) vs. sampling efficiency τ_θ in the digit-pattern example from Fig. 4a–c and Sec. S2 C. The panels show results for different numbers of hidden units N as indicated. Hyperparameters: $n_{CD} = 1$, $\eta = 0.005$, $B = 100$, $|S| = 50\,000$. For observables depending on the visible-unit indices i, i_1, i_2 , the data are averaged over all those indices. Furthermore, as in the main text, each data point is an average over five independently trained RBMs at a fixed training epoch t . The gray dashed line shows the function $\tau_\theta^{(f)} = \tau_\theta$ for reference.

ables in the digit-pattern example from Fig. 4a–c and Sec. S2 C. We remark that, due to the distinct geometry, some of the observables do not have the same physical meaning as in the TFIC example; for instance, $x_i x_{i+1}$ is a correlation function between nearest neighbors along the columns only.

Finally, for a more direct visualization of correlations between samples of Markov chains like (S1), we show snapshots from such chains for RBMs trained on the MNIST dataset in Fig. S6. The autocorrelation-time estimate τ_θ conforms nicely with the number of steps needed

to reach a sample that looks “new” or “uncorrelated” to the naked eye. The adequacy of τ_θ to quantify correlations between Markov-chain samples and to estimate the additional steps required to obtain an independent sample is thus reinforced.

S5. EXTENDED MECHANISM

We expand on aspects of the discussion in the section “Mechanism” from the main text.

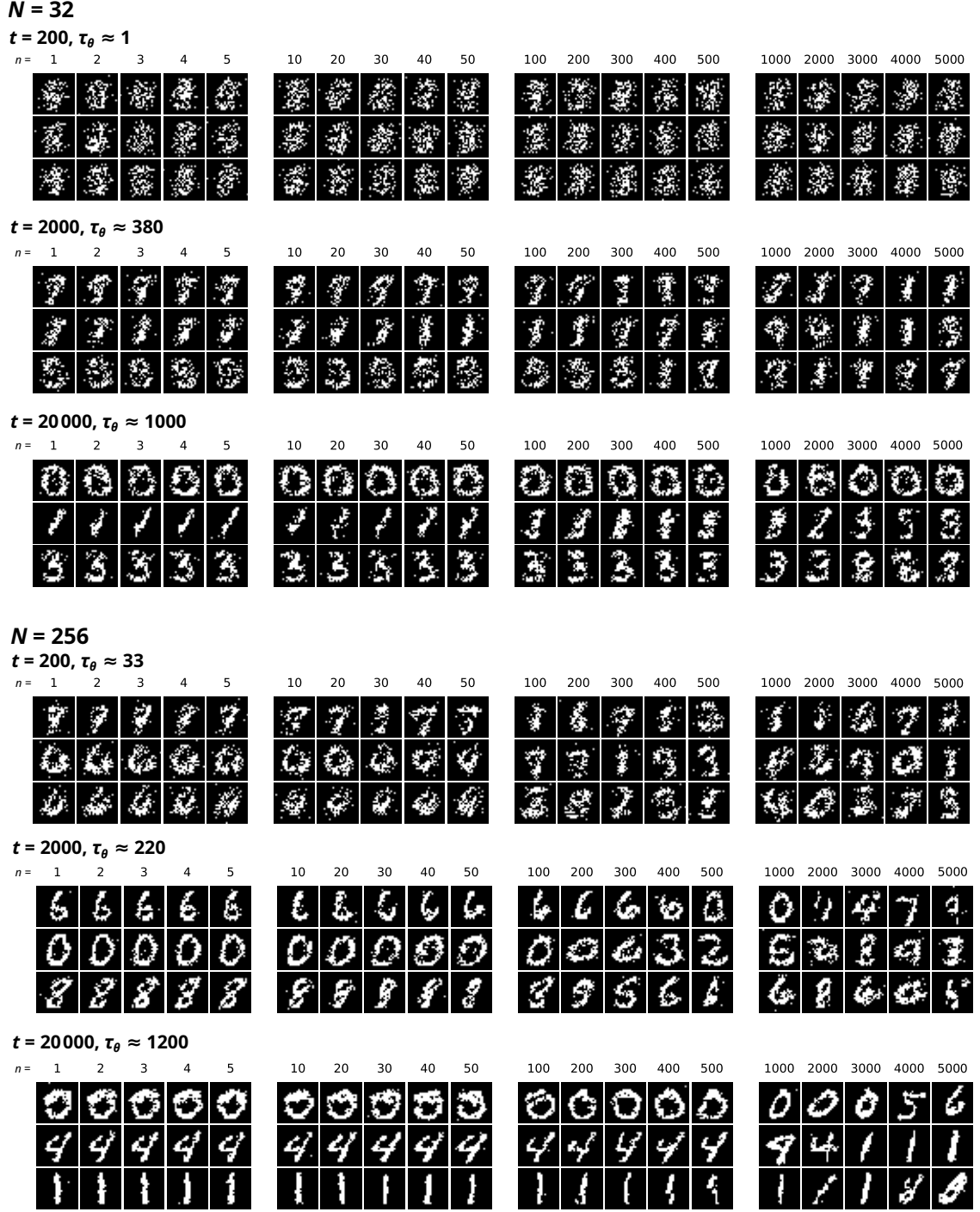


FIG. S6. Example Markov chains obtained from RBMs trained on the MNIST dataset with the PCD algorithm and $n_{\text{CD}} = 1$, $\eta = 10^{-4}$, $B = 100$ for different numbers of hidden units N and training epochs t . All chains were initialized with a uniform random distribution of the visible units x_i [i.e., $p(x_i = 0) = p(x_i = 1) = \frac{1}{2}$] and subsequently thermalized for 2×10^6 steps before recording starts.

A. Minimal loss for independent units

Indeed, if $\hat{p}(x) := \prod_i \hat{p}_i(x_i)$, we can make the following

As stated around Eq. (8) of the main text, the exact loss $\Delta_\theta = D_{\text{KL}}(p \parallel \hat{p}_\theta)$ is bounded from below by the total correlation $C_{\text{tot}}(p)$ if \hat{p}_θ consists of independent units.

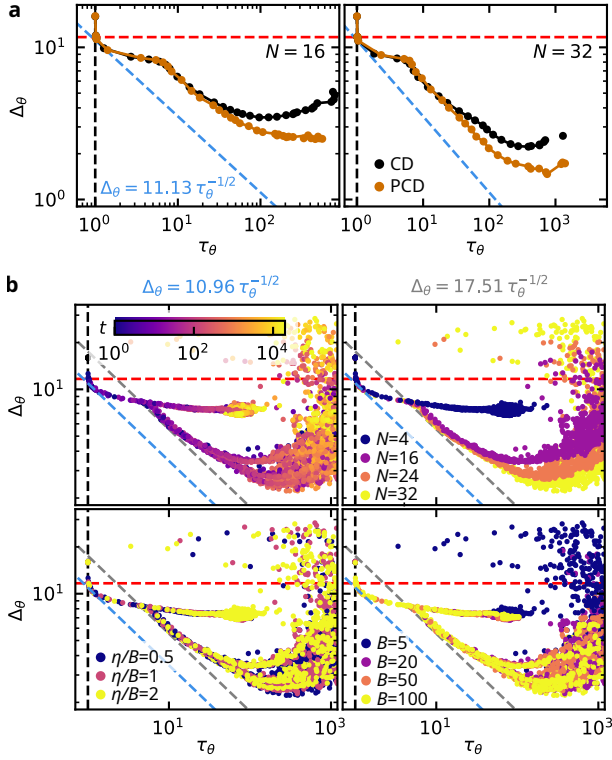


FIG. S7. Exact loss Δ_θ vs. autocorrelation time τ_θ for RBMs in the digit-generator example from Fig. 4a–c and Sec. S2 C. Training used a dataset of $|S| = 50\,000$ samples. Data points are averages over 5 independent runs. (a) Comparison of ordinary contrastive divergence (CD) and persistent contrastive divergence (PCD) with $n_{CD} = 1$, $\eta = 0.005$, $B = 100$ for $N = 16$ (left) and $N = 32$ (right). (b) CD training with $n_{CD} = 1$ and $N = 4, 16, 24, 32$, $\eta/B = 0.5, 1, 2$, $B = 5, 20, 50, 100$. All panels show the same data points, but highlight different hyperparameter dependencies by color and brightness as indicated. Overlapping curves of different colors thus signal that the learning characteristics are independent of the respective hyperparameter.

decomposition:

$$\begin{aligned}
 D_{KL}(p||\hat{p}) &= \sum_x p(x) \left[\log \frac{p(x)}{\prod_i p_i(x_i)} + \log \frac{\prod_i p_i(x_i)}{\prod_i \hat{p}_i(x_i)} \right] \\
 &= \sum_x p(x) \log \frac{p(x)}{\prod_i p_i(x_i)} \\
 &\quad + \sum_i \sum_{x_i} p_i(x_i) \log \frac{p_i(x_i)}{\hat{p}_i(x_i)} \\
 &= C_{\text{tot}}(p) + \sum_i D_{KL}(p_i||\hat{p}_i).
 \end{aligned}$$

Recalling the definition (8) and the fact that $D_{KL}(p||q) \geq 0$ for arbitrary distributions p and q , we can conclude that $D_{KL}(p||\hat{p}) \geq C_{\text{tot}}(p)$.

B. Hyperparameter independence of the tradeoff relation

In the main text, we argued that the relationship between Δ_θ and τ_θ in the independent- and correlation-learning regimes is essentially independent of the basic RBM hyperparameters, including the learning rate η , the batch size B , the number of training samples $|S|$, the number of hidden units N , and the approximation scheme for model averages during training (CD vs. PCD and their order n_{CD}). Further evidence for this insensitivity is provided in Fig. S7 for the digit-generator example from Fig. 4a–c and Sec. S2 C.

We emphasize that the choice of appropriate hyperparameters is still important, because it affects the stability of training and the onset of the degradation regime, meaning that poor choices can lead to early deterioration of the RBMs.

C. Scaling of weights and correlations

The magnitude $|\theta_k|$ of the RBM parameters typically grows during training. A distinctive property of many “real-world” machine-learning problems is that the target distribution is sparse, meaning that most states x have vanishing or at least very small probability $p(x)$. For example, the overwhelming majority of all possible images with a given number of pixels will not display “realistic” motifs (e.g., digits, letters, animals, clothes, buildings, ...). This characteristic is at odds with the RBM model family, which assigns a finite probability $\hat{p}_\theta(x) > 0$ to all states x . To suppress the unlikely states, many of the parameters θ_k have to take large absolute values.

As argued around Eq. (11) and illustrated in Fig. S8, this usually increases the correlations between subsequent Markov-chain samples. Notably, correlations between visible and hidden units, and thus between two (or more) visible units, arise only if $|w_{ij}| > 0$. Hence larger $|\theta_k|$ and larger $|w_{ij}|$ in particular hint at larger autocorrelation times τ_θ . Note, however, that $|w_{ij}| > 0$ for some i, j is not sufficient to obtain correlations between different visible units; to this end, two visible units x_{i_1} and x_{i_2} must be coupled to the same hidden unit h_j , i.e., both $|w_{i_1 j}| > 0$ and $|w_{i_2 j}| > 0$ must hold.

Since it is computationally demanding to estimate τ_θ reliably, the standard deviation $\sigma_w := (\frac{1}{MN-1} \sum_{i,j} w_{ij}^2)^{1/2}$ can be considered as a more accessible indicator of growing correlations in practice. In Fig. S8, we show the mutual dependence of τ_θ and σ_w for the examples from Sec. S2 A–S2 C and various numbers of hidden units N . We observe that the two quantities are indeed positively correlated, which confirms, in particular, that τ_θ typically grows with the magnitude of the weights.

The necessity to increase the RBM parameters θ_k in magnitude in order to represent sparse distributions with many “inactive” states x such that $p(x) = 0$ is also

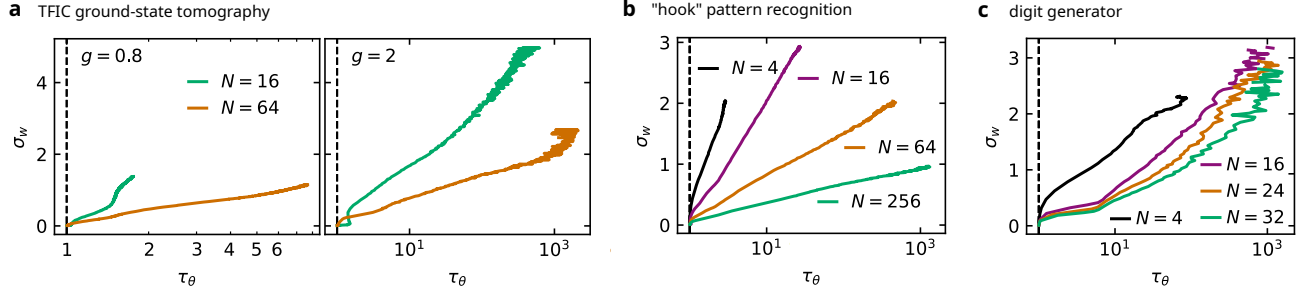


FIG. S8. Standard deviation $\sigma_w := (\frac{1}{MN-1} \sum_{i,j} w_{ij}^2)^{1/2}$ of the weights w_{ij} vs. integrated autocorrelation time τ_θ for RBMs trained with contrastive divergence of order $n_{CD} = 1$ on three different problems. (a) Ground-state tomography in the transverse-field Ising chain of $M = 20$ sites (cf. Fig. 2 and Sec. S2 A), $|S| = 25\,000$, $\eta = 10^{-3}$, $B = 100$, different N and g as indicated. (b) Pattern-recognition task (cf. Fig. 3 and Sec. S2 B), $|S| = 5000$, $\eta = 0.005$, $B = 100$, different N as indicated. (c) Digit generator (cf. Fig. 4a–c and Sec. S2 C), $|S| = 50\,000$, $\eta = 0.005$, $B = 100$, different N as indicated.

one possible hint at the source of the different α values observed in Fig. 2d compared with Fig. 2b (and also Figs. 3b and 4b,c). The image distributions from Figs. 3a–c and 4b,c all have a large fraction of such “inactive” states (99.92 % and 99.88 %, respectively, see Secs. S2 B and S2 C). Likewise, the TFIC ground state in the σ^z basis (when $\alpha = \frac{1}{2}$) has $p(x) = 0$ for half of the states by symmetry (see Sec. S2 A and S5 D), whereas no such inactive states exist in the σ^x representation (when $\alpha = 6 \dots 8$).

Within the examples from Fig. 2d, the case with $g = 1$ stands out because it also exhibits a pronounced intermediate stage in the correlation-learning regime where the relationship between Δ_θ and τ_θ does not follow the power-law tradeoff of the global bound with $\alpha \simeq 6$, but instead shows a stronger tradeoff with $\alpha \simeq \frac{1}{4}$. A more detailed analysis (see Sec. S5 D) suggests that this is caused by the emerging strong bimodal structure of the target distribution as g becomes smaller, which impedes and eventually prevents efficient learning.

D. Basis-dependent learning characteristics in the transverse-field Ising chain

We investigate the emergence of an intermediate stage in the correlation-learning regime, where learning is less efficient than admitted by the global power-law tradeoff, in the example of ground-state tomography for the transverse-field Ising chain in the σ^x basis as g becomes smaller (see, in particular, Fig. 2d of the main text).

Since there are some important differences in the learning characteristics of the TFIC ground-state distribution in the σ^z and σ^x bases (cf. Figs. 2b and d), we first examine the underlying target distribution $p(x)$ in more detail. To avoid confusion in the following, we denote the target distribution as $p^z(x)$ when referring to the σ^z basis representation and as $p^x(x)$ when referring to the σ^x basis representation. The Hamiltonian (S7) has a \mathbb{Z}_2 symmetry of the form $F := \prod_i \sigma_i^z$, i.e., $[H, F] = 0$. In the σ^z basis, F measures the parity of the number of down

spins, whereas it describes a spin-flip symmetry in the σ^x basis.

For even M , to which we restrict our discussion exclusively in this work, the ground state (S12) of the Hamiltonian (S7) lies in the $F = +1$ sector. In the σ^z basis, this means that $p^z(x) = 0$ for half of the basis states, namely all configurations $x = (x_1, \dots, x_M)$ for which $\sum_i x_i$ is odd. In the σ^x basis, by contrast, it implies that $p^x(x) = p^x(1 - x)$, where $1 - x = (1 - x_1, \dots, 1 - x_M)$. This distinct manifestation of the symmetry F is the first important distinction between the σ^z - and σ^x -basis representations. Learning the σ^x representation is thus aided by the fact that the RBM model can encode *relative* spin orientations (alignment or anti-alignment) particularly efficiently, requiring only a single hidden unit for an arbitrary combination of visible ones, although the effectively needed number of weights appears to depend also on the proximity to the critical point [S9]. By contrast, due to the exponential form of the model distribution, it is rather inefficient at enforcing $\hat{p}_\theta(x) = 0$ for individual states x as required by the σ^z representation $p^z(x)$. These observations hint at possible origins of the different exponents α in the tradeoff relation (7) for the two representations, a large value $\alpha \simeq 6 \dots 8$ for the better suited $p^x(x)$ and a small value $\alpha \simeq \frac{1}{2}$ for the worse suited $p^z(x)$.

For large values of g , $p^z(x)$ is dominated by the state $x = (0, \dots, 0)$ (“all spins up”), while $p^x(x)$ becomes approximately uniform. For small values of g , in turn, $p^z(x)$ approaches a uniform distribution, whereas $p^x(x)$ is dominated by the two states $x = (0, \dots, 0)$ and $x = (1, \dots, 1)$, whose probability is degenerate due to the symmetry F . The different mode structure in the nonuniform limit of the σ^z - and σ^x -basis representations is a second important difference between them. Strongly unimodal as well as approximately uniform distributions are structurally simple, and gradient-descent training can find a globally optimal solution relatively easily. If the distribution has two (or a few) modes or dominant states, by contrast, the risk of getting stuck in a local minimum of the loss landscape and detecting only a subset of those dominant

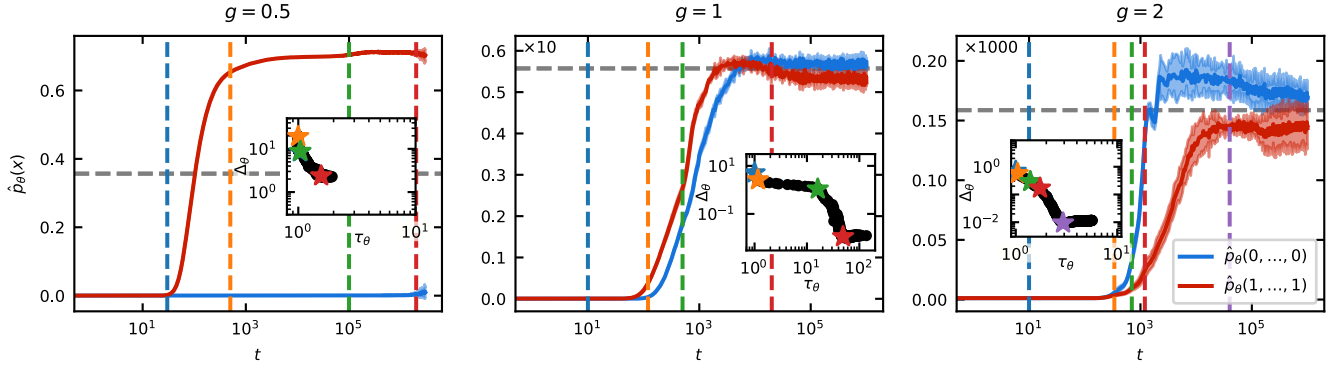


FIG. S9. Evolution of the model probabilities $\hat{p}_\theta(x)$ with the training time t for the two dominant states of the target distribution $p^x(x)$, $x = (0, \dots, 0)$ (all spins up, blue) and $x = (1, \dots, 1)$ (all spins down, red). Horizontal dashed lines show $p^x(x)$ for those states. Shaded areas indicate the fluctuations across five independent runs (standard deviation). Training used contrastive divergence of order $n_{CD} = 1$ and hyperparameters as in Fig. 2d of the main paper, i.e., $\eta = 10^{-3}$, $B = 100$, $|S| = 25\,000$. Insets: Exact loss Δ_θ vs. autocorrelation time τ_θ . Selected epochs are marked by colored vertical dashed lines in the main panel and stars in the insets. Note the scaling of the y -axis in the middle and right panels as indicated in the top-left corner.

states is increased.

We presume that the bimodal structure of $p^x(x)$, which becomes increasingly pronounced as g becomes smaller, is the reason for the intermediate stage in the correlation-learning regime observed in the top panel ($g = 1$) of Fig. 2d. To substantiate this claim, we investigate the evolution of the model probability $\hat{p}_\theta(x)$ during training for the two modes $x^+ := (0, \dots, 0)$ and $x^- := (1, \dots, 1)$. Fig. S9 shows these probabilities for three different values of g .

We focus on the middle panel ($g = 1$) first, where $p^x(x^\pm) \approx 5.6\%$. The end of the correlation-learning regime is marked by the blue dashed line (blue star in the inset). Thereafter, the RBM first picks up the x^-

mode, accompanied by a segment with $\alpha \simeq 6$ (see also Fig. 2d in the main text). The probability of the other mode x^+ only starts to increase slightly later at around the orange mark, which also corresponds to the starting point of the second stage of correlation learning with $\alpha \simeq \frac{1}{4}$. It lasts until both modes are established (green mark), and the subsequent fine tuning proceeds with a more efficient tradeoff exponent of $\alpha \simeq 6$ again. A similar, but less pronounced behavior can be observed for $g = 2$ (right panel of Fig. S9), where the two modes only have $p^x(x^\pm) \approx 0.015\%$. On the contrary, if the modes become more pronounced as exemplified by the $g = \frac{1}{2}$ case with $p^x(x^\pm) \approx 36\%$ (left panel), the RBM only learns one of the modes and fails to detect the other one.

[S1] G. E. Hinton, Training products of experts by minimizing contrastive divergence, *Neural Comput.* **14**, 1771 (2002).

[S2] G. E. Hinton, A practical guide to training restricted Boltzmann machines, in *Neural Networks: Tricks of the Trade: Second Edition*, edited by G. Montavon, G. B. Orr, and K.-R. Müller (Springer, Berlin, Heidelberg, 2012) pp. 599–619.

[S3] T. Tieleman, Training restricted Boltzmann machines using approximations to the likelihood gradient, in *Proceedings of the 25th International Conference on Machine Learning*, ICML '08 (Association for Computing Machinery, New York, NY, USA, 2008) p. 1064–1071.

[S4] A. Fischer and C. Igel, An introduction to restricted Boltzmann machines, in *Progress in Pattern Recognition, Image Analysis, Computer Vision, and Applications*, edited by L. Alvarez, M. Mejail, L. Gomez, and J. Jacobo (Springer, Berlin, Heidelberg, 2012) pp. 14–36.

[S5] G. Montúfar, Restricted Boltzmann machines: Introduction and review (2018), arXiv:1806.07066.

[S6] L. Vidmar and M. Rigol, Generalized Gibbs ensemble in integrable lattice models, *J. Stat. Mech: Theory Exp.* **2016**, 064007 (2016).

[S7] G. Torlai, G. Mazzola, J. Carrasquilla, M. Troyer, R. Melko, and G. Carleo, Neural-network quantum state tomography, *Nat. Phys.* **14**, 447 (2018).

[S8] Y. LeCun, C. Cortes, and C. J. C. Burges, The MNIST database of handwritten digits, <http://yann.lecun.com/exdb/mnist/>.

[S9] A. Golubeva and R. G. Melko, Pruning a restricted Boltzmann machine for quantum state reconstruction (2021), arXiv:2110.03676.